J. Fluid Mech. (2005), *vol.* 535, *pp.* 33–64.
doi:10.1017/S0022112005004532 Printed in the United Kingdom

Analytical evolution of tsunamis induced by near-shore earthquakes on a constant-slope ocean

By STEFANO TINTI AND ROBERTO TONINI

Department of Physics, Sector of Geophysics, University of Bologna, Italy

(Received 29 March 2004 and in revised form 24 January 2005)

Strong near-shore earthquakes are the most frequent sources of tsunamis in many oceans of the world. In the framework of the nonlinear shallow-water theory, the initial sea-surface tsunami elevation is assumed to equal the sea-floor co-seismic displacement produced by the seismic event. This is quantified by means of the analytical formulas due to Okada (1985, 1992), dealing with seismic faults buried in an elastic medium. In this work the propagation of tsunamis is studied along two-dimensional profiles on an idealized constant-slope sea bed, an approximation that allows one to reduce the governing nonlinear equations to a linear problem by means of the classical Carrier & Greenspan (1958) approach. We introduce an analytical solution that is sufficiently general to account for initial conditions associated with paradigmatic cases of sea-bottom deformations produced by near-shore earthquakes, such as subsidence or uplift of the coastal area, and can be also used to treat more complex deformations. The main result is that the amplification of the tsunami height at the coast is found to range between approximately 1 and 2. The amplification is around 1 for tsunamis induced by earthquakes with their epicentre inland and tends to grow as the fault moves seaward. We restrict our analysis to earthquakes that dislocate the shore region. Within the class of sources that we consider, the tsunamis that are most amplified are the ones having initial profiles with a crest–trough–crest system or conversely with a trough–crest–trough system. The bottom slope is found to have no effect on tsunami run-ups and run-downs, but to influence tsunami periods and tsunami speed remarkably. Breaking analysis shows that wave breaking does not occur if the initial wave height is less than 8–9 m, and that the simplest sea-level profiles, which are associated with earthquakes with their epicentre on land, are not expected to break even if their initial height exceeds 19 m.

1. Introduction

The most frequent source of tsunamis is submarine earthquakes that offset and/or deform the sea floor over very large regions, extending tens/hundreds of kilometres in length and width. Often the seismic sources are in association with subduction zones in deep ocean trenches that are far from the coasts, such as the Tonga and Mariana trenches in the Pacific. But equally often the earthquakes occur only a few tens of kilometres from coasts or in coastal regions where they may cause permanent changes in the shoreline position as the effect of coastal subsidence and uplift. One finds examples of tsunamigenic earthquakes that took place in near-shore zones in various regions of the world.

To stress the relevance of such occurrences, it suffices to mention here some recent and significant cases of destructive events, all characterized by seismic deformations involving the coast: the December 12, 1992 Flores, Indonesia tsunami, that was produced by an $M_w = 7.8$ earthquake just off the northern coast of the island (Yeh *et al.* 1993); the July 12, 1993 Okushiri, Japan tsunami, that was caused by an $M_w = 7.8$ earthquake in the Hokkaido-Nansei-Oki region in the Japan sea (Hokkaido Tsunami Survey Group 1993; Shuto & Matsutomi 1995); the August 19, 1999 zmit Bay, Turkey tsunami, that was set up by an $M_w = 7.4$ earthquake rupturing several segments of the North Anatolian Fault with epicentre located near the coastal town of Gölcük (Yalçiner *et al.* 2001; Altinok *et al.* 2001); and the June 23, 2001 Camana-Chala, Peru tsunami, that was generated by an $M_w = 8.4$ shock, 110 miles west of Arequipa in the Pacific Ocean earthquake (International Survey Team 2001; Geist *et al.* 2001). Here, M_w is the moment magnitude as defined by Hanks & Kanamori (1979). In some regions of the world, near-coast tsunamigenic earthquakes are by far the most frequent sources of tsunamis. An example is provided by the Mediterranean sea, where tsunami catalogues, going back more than 2000 years and probably complete for the last four centuries, show that tsunamis produced by far sources are rare (see Tinti & Maramai 1996, and Tinti, Maramai & Graziani 2004, for the Italian tsunamis; Soloviev *et al.* 2000, and Maramai, Graziani & Tinti 2003, for tsunamis in the Mediterranean and in other European seas).

In this paper attention is focused on the propagation of tsunamis generated in the coastal zone. This subject has gained wide interest after recent episodes of destructive events that have proven the damaging potential of local tsunamis, and have also shown the need of devising more efficient means and methods to protect coastal communities from their attacks (Preuss, Raad & Bidoae 2001). Our purpose is to compute near-source tsunami evolution, as well as tsunami run-up and run-down, and the corresponding tsunami penetration and withdrawal, in relation to the characteristics of the co-seismic dislocation of the coast determined by the near-shore earthquake. In order to gain basic physical understanding, we will make use of an idealized bathymetry, namely a constant-slope sea floor, since this allows simplification of the governing equations and of the consequent mathematical treatment, but implies no loss of generality. And we will also consider only simple idealized seismic sources that are capable of producing either uplift or subsidence of the near-shore sea bed, or some slightly more complicated deformation pattern. The seismic deformations of the sea bottom will be calculated through the analytical formulas deduced by Okada (1992), providing the inner and Earth-surface displacements generated by a rectangular uniform-slip fault buried in a homogeneous elastic half-space.

The tsunami propagation will be studied along transects perpendicular to the coast, by using the two-dimensional nonlinear shallow-water approximation of the Navier–Stokes hydrodynamic equations. The link between the co-seismic sea-floor displacement and the ensuing tsunami is usually assumed to be that (i) the initial vertical displacement of the sea surface is equal to the vertical displacement of the sea bottom and (ii) the initial velocity of the sea water is zero everywhere. These assumptions are justified by the consideration that co-seismic deformations take place over very large areas (with typical length much larger than the local sea depth) and within a very short time (seismic ruptures and disturbances travel much faster than tsunami waves), and are widely accepted in all studies of tsunamis generated by earthquakes. Conversely, they may be questionable for tsunamis caused by smaller-scale and slower sources, such as submarine mass movements (Trifunac & Todorovska 2003). Based on the approach devised by Carrier & Greenspan (1958), we have found a new analytical

solution to the two-dimensional nonlinear shallow-water equations that is sufficiently general to cover a wide variety of initial sea-surface profiles. We will use this solution to treat the paradigmatic cases of initial sea-level depression and rise that are associated respectively with sea-floor subsidence and uplift due to coastal seismic sources.

2. Co-seismic deformation induced by coastal earthquakes

Earthquakes give rise to permanent deformations of the Earth's surface that depend on the focal mechanism and on the properties of the crust. In spite of the complications of the seismic source and of the internal structure of the Earth, assuming a simple geometry both for the source and the media has proven to be successful in providing useful and practical assessments of the displacements. The most widely used set of formulas is the one deduced by Okada (1985, 1992) that allows one to quantify the displacements produced in a perfectly elastic half-space by a rectangular fault having the upper edge parallel to the Earth's surface, and with uniform slip distribution. In this study we will only consider shear dislocations, which are appropriate for earthquake sources. Furthermore, since we will restrict ourselves to a two-dimensional analysis, we will take into consideration faults of infinite aspect ratio (i.e. with infinite length and finite width), and with only a dip-slip focal mechanism (i.e. with no slip component along the strike direction). Since Okada's formulas are for finite rectangular faults, some computations are needed to deduce the expressions suitable for infinitely long faults; these are performed in Appendix A. A vertical two-dimensional dip-slip fault produces a typical dipole pattern, with positive and negative vertical surface displacements, which possesses an antisymmetric distribution on the two sides of the fault. If the fault is offshore, the perturbation region is totally or predominantly submarine, and the initial tsunami wave conserves the dipole configuration. But if the source is close to the coast, or inland, then only part of the dislocation involves the sea floor, and the antisymmetry of the pattern is destroyed. Figure 1 shows that, depending on the relative positions of the seismic source and the shoreline, the sea bottom can be affected by uplift only (or subsidence) with maximum displacement taking place at the coastline or at some distance offshore, or it can be affected by both uplift and subsidence. Okada's formulas show that there is a linear relationship between the displacement field and the amount of the offset on the fault's surface: therefore, varying the fault slip does not alter the co-seismic deformation pattern, only its magnitude (figure 2*a*). On the other hand, the antisymmetric pattern associated with a vertical fault ($\mathrm{dip} = 90^\circ$) changes with the dip angle of the fault (figure 2*b*): an inclined inverse (normal) fault produces surface displacement fields with predominant uplift (subsidence). Since the sea bottom profile transfers to the initial sea surface unaltered, we have to devise a tsunami model that can handle all these cases. Fault parameters used to obtain the profiles displayed in figures 1 and 2 are listed in table 1.

3. Nonlinear tsunami theory in a two-dimensional space

Exact solutions to the nonlinear shallow-water equations for non-breaking waves were found in 1958 by Carrier & Greenspan (1958, referred to herein as CG) under the assumption of a sea bed with uniform slope. They were able to transform the problem, involving linear momentum and mass conservation equations, into a single linear second-order differential equation of hyperbolic type, and worked out some examples

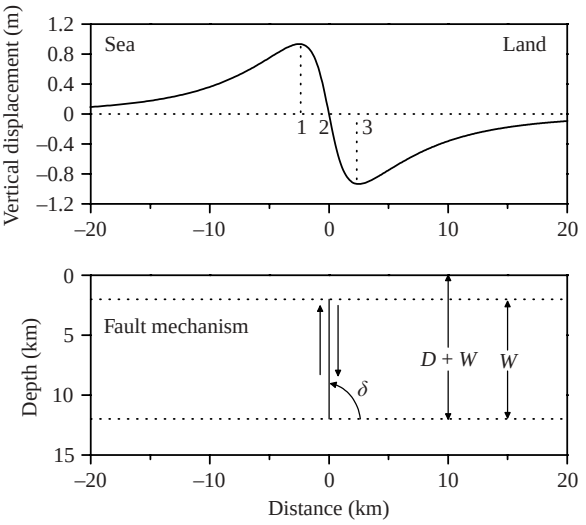

FIGURE 1. Plot of the vertical displacement of the Earth's surface produced by a vertical fault (dip angle $\delta = 90°$) in homogeneous ground. The fault has width W and its upper edge is at depth D. The left block shifts upward and the right block shifts downward an equal amount. The theory predicts an antisymmetric displacement field with respect to the fault plane. The sea floor experiences vertical movements that depend on the relative position of the fault and the coastline. If the shoreline is at position 1, the sea bed is uplifted with maximum uplift at the shoreline. If it is at position 2, the shoreline does not move, but the coastal zone is tilted, with the ocean floor uplifted and the land subsiding. If it is at position 3, the sea bed is both uplifted at large distance offshore, and subsiding near-shore. In cases 1 and 3 the shoreline position changes permanently.

	Figure 1	Figure 2(*a*)	Figure 2(*b*)	Figure 4 Case 1	Figure 4 Case 2	Figure 4 Case 3	Figure 4 Case 4 Fault 1	Figure 4 Case 4 Fault 2	Figure 4 Case 4 Fault 3
Fault									
Width (km)	10	10	10	10	10	10	7	22	5
Dip (deg.)	90	90	50, 70, 90	90	90	90	80	70	90
$\mathrm{UEP}^{(A)}x$ (km)	0	0	0	1.90	0	−0.6	−0.95	1.82	0.05
$\mathrm{UEP}^{(A)}z$ (km)	2.00	2.00	2.00	2.00	2.00	2.00	1.50	7.92	0.90
$\mathrm{Slip}^{(B)}$ (m)	3.00	1, 2, 3	3.00	3.21	3.21	3.21	3.00	2.50	−4.40

TABLE 1. Fault parameters (A) The faults are rectangular surfaces with strike parallel to the y-axis, and with the upper edge that is horizontal and of infinite length. They are symmetrical with respect to the x-axis. UEP stands for upper edge position. The origin of the x-axis is taken here to correspond with the position of the pre-earthquake coastline. The z-coordinate is the depth and is positive downward. (B) The slip is the relative displacement of the two sides of the fault, which each move by one half of the slip in opposite directions.

with specific initial-value conditions. Later, Spielvogel (1975) applied CG's approach to compute the amplification of a special class of waves that at the run-up time do not possess kinetic energy and exhibit an exponential sea-level profile, and Synolakis (1987) used CG's theory to study the run-up of a solitary wave travelling over a flat-bottom ocean and climbing over a constant-slope beach. Tadepalli & Synolakis (1994) extended Synolakis's analysis to cover N-waves with leading depression and

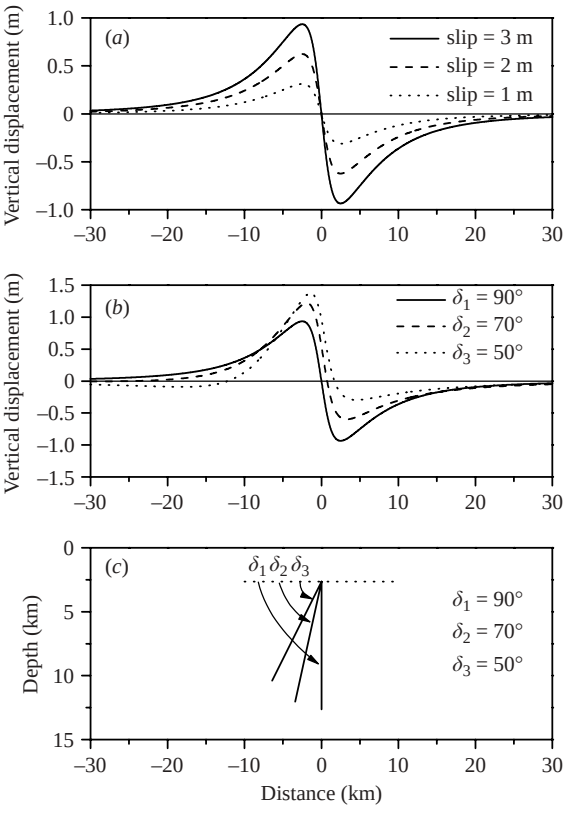

FIGURE 2. Effect of (*a*) slip and fault dip (*b*) on the vertical co-seismic displacements. The position and the dip of the faults are sketched in (*c*). According to the theory, displacements depend linearly on the amount of the slip on the fault. Reversing the slip changes the sign of the displacements, and uplift switches to subsidence and vice versa. The inclined faults are thrust (inverse) faults with the headwall (left-side block) uplifting and the footwall subsiding. Varying the fault dip breaks the antisymmetry of the vertical fault displacements: near-fault uplift prevails over subsidence.

leading elevation. Recently, Carrier, Wu & Yeh (2003) reconsidered and modified CG's original approach and provided a general solution technique accounting for arbitrary initial-value conditions, i.e. for arbitrary initial water elevation and velocity profiles, and Kânoğlu (2004) contributed to the appropriate definition of the initial conditions. The related techniques are semi-analytical, in that numerical integration is needed to obtain a solution in the space and time domain.

In this section we will follow the basic philosophy of the original CG analysis, which means that we will introduce new exact solutions to the problem. This will enable us to use simple analytical formulas to compute the evolution of the elevation and of the velocity fields, and all other quantities that have physical and engineering interest, such as the displacement of the shoreline, the wave run-up and draw-down, etc. Tsunamis are long water waves propagating in an ocean with depth negligible compared to the wavelength, and can be described by the two nonlinear shallow-water equations:

$$(v^*(\eta^* + h^*))_{x^*} = -\eta^*_{t^*}, \tag{3.1}$$

$$v^*_{t^*} + v^* v^*_{x^*} = -g\eta^*_{x^*}, \tag{3.2}$$

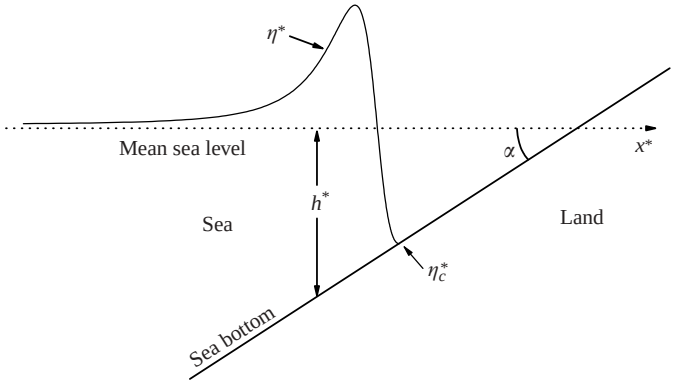

FIGURE 3. Plot of the constant-slope ocean and of the dimensional variables used. The x^*-coordinates increase landward, and the post-earthquake shoreline is placed at the origin. η_c^* is the instantaneous coastline position. The coastal earthquake produces a local permanent change in the sea floor, but it is assumed here to have an extent too limited to affect the mean sea level, which does not change.

where η^* is the water elevation with respect to the mean sea level, v^* is its horizontal velocity, g is gravitational acceleration, $h^* = -bx^*$ is the local mean depth, and x^* is the horizontal coordinate. In still water, the coastline is located at $x^* = 0$ and the ocean is found in the region of negative x^* (see figure 3). Let us introduce the following dimensionless quantities:

$$v = v^*/v_0, \tag{3.3}$$

$$x = x^*/l_0, \tag{3.4}$$

$$\eta = \eta^*/bl_0, \tag{3.5}$$

$$t = t^*/T, \tag{3.6}$$

where $T = (l_0/bg)^{1/2}$, $v_0 = (bl_0 g)^{1/2}$, $b = \tan\alpha$, α being the inclination of the slope (see figure 3), and l_0 is a characteristic length that can be determined for each specific problem. After using the above scaling laws, the set of equations (3.1) and (3.2) can be written in terms of the dimensionless variables as

$$(v(\eta - x))_x + \eta_t = 0, \tag{3.7}$$

$$v_t + vv_x + \eta_x = 0. \tag{3.8}$$

3.1. *From the nonlinear to the linear problem*

Following CG, the fully nonlinear equations (3.7) and (3.8) in the space and time dimensionless variables x, t can be converted into a linear problem in a new pair of independent variables σ, λ by using the nonlinear hodograph transformation, defined as follows:

$$v = \frac{\phi_\sigma}{\sigma}, \tag{3.9}$$

$$x = \frac{\phi_\lambda}{4} - \frac{\sigma^2}{16} - \frac{v^2}{2}, \tag{3.10}$$

$$\eta = \frac{\phi_\lambda}{4} - \frac{v^2}{2}, \tag{3.11}$$

$$t = \frac{\lambda}{2} - v, \tag{3.12}$$

where $\phi(\sigma, \lambda)$ plays the role of a field potential. The following linear second-order differential equation in terms of the water velocity $v(\sigma, \lambda)$, defined in the plane (σ, λ), is obtained after some mathematical manipulations:

$$\sigma(v_{\sigma\sigma} - v_{\lambda\lambda}) + 3v_{\sigma} = 0. \tag{3.13}$$

Analogously, one can deduce an equivalent linear equation for the potential $\phi(\sigma, \lambda)$, that is

$$(\sigma\phi_{\sigma})_{\sigma} - \sigma\phi_{\lambda\lambda} = 0. \tag{3.14}$$

3.2. *The initial-value problem*

By virtue of the transformation law (3.12), it is easy to see that imposing that the water velocity vanishes identically on the axis $\lambda = 0$ implies that the axis $\lambda = 0$ and the axis $t = 0$ are exactly superimposed. Therefore, an initial-value problem in x and t space with zero water velocity can be mapped to an equivalent problem in the plane (σ, λ) in a straightforward manner. If the initial conditions are written as

$$v(\sigma, \lambda = 0) = 0, \tag{3.15}$$

$$v_{\lambda}(\sigma, \lambda = 0) = f(\sigma), \tag{3.16}$$

where $f(\sigma)$ is an arbitrary function, then a general integral solution can be found both for v and for ϕ (see CG):

$$v(\sigma, \lambda) = \sigma^{-1} \int_0^{\infty} J_1(\tau\sigma) \sin(\tau\lambda) \left(\int_0^{\infty} \sigma_0^2 J_1(\tau\sigma_0) f(\sigma_0)\, \mathrm{d}\sigma_0 \right) \mathrm{d}\tau, \tag{3.17}$$

$$\phi(\sigma, \lambda) = -\int_0^{\infty} \tau^{-1} J_0(\tau\sigma) \sin(\tau\lambda) \left(\int_0^{\infty} \sigma_0^2 J_1(\tau\sigma_0) f(\sigma_0)\, \mathrm{d}\sigma_0 \right) \mathrm{d}\tau. \tag{3.18}$$

Here J_0 and J_1 are Bessel functions of the first kind and of order zero and one, respectively.

At first sight, specifying the appropriate function $f(\sigma)$ for a given tsunami problem seems to be not trivial, but the following considerations are of some help. After differentiating both sides of equation (3.9) with respect to λ and both sides of equation (3.11) with respect to σ, we obtain

$$v_{\lambda}(\sigma, \lambda) = \phi_{\sigma\lambda}/\sigma,$$

$$\eta_{\sigma}(\sigma, \lambda) = \phi_{\lambda\sigma}/4 - v v_{\sigma}.$$

Then, combining them at $\lambda = 0$, we obtain the relationship

$$v_{\lambda}(\sigma, 0) = f(\sigma) = \frac{4}{\sigma} \eta_{\sigma}(\sigma, 0), \tag{3.19}$$

which shows the link existing between the function $f(\sigma)$ and the initial sea-surface profile $\eta(\sigma, 0)$.

3.3. *The new exact solution*

We find it convenient to consider the following form for the initial profile $\eta(\sigma, 0)$, since it will prove to be sufficiently flexible to represent relevant cases of initial sea-surface disturbances due to near-shore earthquakes:

$$\eta(\sigma, 0) = (1 + \sigma^2)^{-3/2} \sum_{k=0}^{3} c_k (1 + \sigma^2)^{-k}, \tag{3.20}$$

where c_k are four arbitrary coefficients. We remark that expression (3.20) may be seen as the generalization of a simpler form already analysed in CG. From equation (3.19), we may easily compute the function $f(\sigma)$:

$$f(\sigma) = \frac{4}{\sigma}\eta_\sigma(\sigma, 0) = -8(1+\sigma^2)^{-5/2}\sum_{k=0}^{3}\left(\tfrac{3}{2}+k\right)c_k(1+\sigma^2)^{-k}, \tag{3.21}$$

which can be substituted in the double integral of expressions (3.17) and (3.18) to provide the solutions for the velocity v and for the potential ϕ. Details on the computation of these integrals are given in Appendix B. Further, the analytical expression for the water elevation η can be obtained by making use of the transformation law (3.11). The analytical formulas we found can be written as follows:

$$\begin{aligned} v(\sigma,\lambda) = &-4\left(c_0+\frac{c_1}{3}+\frac{c_2}{5}+\frac{c_3}{7}\right)\mathrm{Im}\left\{\frac{1}{(p^2+\sigma^2)^{3/2}}\right\} \\ &-4\left(\frac{c_1}{3}+\frac{c_2}{5}+\frac{c_3}{7}\right)\mathrm{Im}\left\{\frac{3p}{(p^2+\sigma^2)^{5/2}}\right\} \\ &-4\left(\frac{c_2}{5}+\frac{6c_3}{35}\right)\mathrm{Im}\left\{\frac{-1}{(p^2+\sigma^2)^{5/2}}+\frac{5p^2}{(p^2+\sigma^2)^{7/2}}\right\} \\ &-4\frac{c_3}{7}\mathrm{Im}\left\{\frac{-3p}{(p^2+\sigma^2)^{7/2}}+\frac{7p^3}{(p^2+\sigma^2)^{9/2}}\right\}, \end{aligned} \tag{3.22}$$

$$\begin{aligned} \phi(\sigma,\lambda) = &\;4\left(c_0+\frac{c_1}{3}+\frac{c_2}{5}+\frac{c_3}{7}\right)\mathrm{Im}\left\{\frac{1}{(p^2+\sigma^2)^{1/2}}\right\} \\ &+4\left(\frac{c_1}{3}+\frac{c_2}{5}+\frac{c_3}{7}\right)\mathrm{Im}\left\{\frac{p}{(p^2+\sigma^2)^{3/2}}\right\} \\ &+4\left(\frac{c_2}{15}+\frac{2c_3}{35}\right)\mathrm{Im}\left\{\frac{-1}{(p^2+\sigma^2)^{3/2}}+\frac{3p^2}{(p^2+\sigma^2)^{5/2}}\right\} \\ &+4\frac{c_3}{35}\mathrm{Im}\left\{\frac{-3p}{(p^2+\sigma^2)^{5/2}}+\frac{5p^3}{(p^2+\sigma^2)^{7/2}}\right\}, \end{aligned} \tag{3.23}$$

$$\begin{aligned} \eta(\sigma,\lambda) = &\left(c_0+\frac{c_1}{3}+\frac{c_2}{5}+\frac{c_3}{7}\right)\mathrm{Re}\left\{\frac{p}{(p^2+\sigma^2)^{3/2}}\right\} \\ &+\left(\frac{c_1}{3}+\frac{c_2}{5}+\frac{c_3}{7}\right)\mathrm{Re}\left\{\frac{-1}{(p^2+\sigma^2)^{3/2}}+\frac{3p^2}{(p^2+\sigma^2)^{5/2}}\right\} \\ &+\left(\frac{c_2}{15}+\frac{6c_3}{35}\right)\mathrm{Re}\left\{\frac{-3p}{(p^2+\sigma^2)^{5/2}}+\frac{5p^3}{(p^2+\sigma^2)^{7/2}}\right\} \\ &+\frac{c_3}{35}\mathrm{Re}\left\{\frac{3}{(p^2+\sigma^2)^{5/2}}+\frac{-30p^2}{(p^2+\sigma^2)^{7/2}}+\frac{35p^4}{(p^2+\sigma^2)^{9/2}}\right\}-\frac{v^2}{2}, \end{aligned} \tag{3.24}$$

where $p = (1 - \mathrm{i}\lambda)$. Equations (3.22)–(3.24) are complemented by a pair of expressions that allows one to convert the solution from the coordinates (σ, λ) to the dimensionless space and time coordinates x and t: namely, the relationship (3.12), linking t and λ, and the relation between x and η that can be easily derived by combining (3.10) with (3.11), that is

$$x(\sigma,\lambda) = \eta(\sigma,\lambda) - \frac{\sigma^2}{16}. \tag{3.25}$$

One of the advantageous properties of the hodograph transformation is that in the space (σ, λ) the shoreline is represented by the axis $\sigma = 0$ at any time. Therefore, putting $\sigma = 0$ in (3.22) and (3.24) allows one to compute respectively the instantaneous velocity v_c of the tip of the wave at the coast, as well as the instantaneous shoreline elevation η_c (and accordingly the shoreline penetration). The explicit formulas are

$$v_c(\lambda) = v(0, \lambda) = -4\left(c_0 + \frac{c_1}{3} + \frac{c_2}{5} + \frac{c_3}{7}\right)\mathrm{Im}\left\{\frac{1}{p^3}\right\} - 4\left(\frac{c_1}{3} + \frac{c_2}{5} + \frac{c_3}{7}\right)\mathrm{Im}\left\{\frac{3}{p^4}\right\} - 4\left(\frac{c_2}{5} + \frac{6c_3}{35}\right)\mathrm{Im}\left\{\frac{4}{p^5}\right\} - 4\frac{c_3}{7}\mathrm{Im}\left\{\frac{4}{p^6}\right\}, \tag{3.26}$$

$$\eta_c(\lambda) = \eta(0, \lambda) = \left(c_0 + \frac{c_1}{3} + \frac{c_2}{5} + \frac{c_3}{7}\right)\mathrm{Re}\left\{\frac{1}{p^2}\right\} + \left(\frac{c_1}{3} + \frac{c_2}{5} + \frac{c_3}{7}\right)\mathrm{Re}\left\{\frac{2}{p^3}\right\} + \left(\frac{c_2}{5} + \frac{c_3}{35}\right)\mathrm{Re}\left\{\frac{2}{p^4}\right\} + \frac{c_3}{35}\mathrm{Re}\left\{\frac{8}{p^5}\right\} - \frac{v_c^2}{2}. \tag{3.27}$$

4. Results and discussion of elementary cases

In order to analyse the evolution of tsunamis generated by near-shore seismic sources, some paradigmatic cases have been considered, and are illustrated in figure 4. Case 1 is a vertical fault located inland at some distance from the shoreline causing sea-bed uplift and downlift of the landward block (figure 4*a*). In case 2, the same vertical fault is placed under the shoreline (figure 4*b*). In case 3 it is located slightly offshore, which causes a narrow coastal belt of the sea floor to subside (with subsidence peak at the coast), and the sea bed to be offset upward offshore (figure 4*c*). A more complex coastal source is considered in case 4, where a dominant inverse two-segment fault, placed under the seabed in the coastal area, is coupled with an ancillary surface normal fault, further inland, to form a graben. The effect is an asymmetrical dipole sea-bottom displacement profile: the coastal zone subsides with the subsidence peak offshore, and the seaward sea floor is displaced upward (figure 4*d*). Since earthquake sources are in the coastal region, the magnitude of the co-seismic displacements dies out moving seaward, and the sea bed is practically unaffected offshore. In the examples of figure 4, the seismic disturbance is almost negligible at distances larger than 75 km. Notice further that the gradient of the vertical displacement is larger at the source and becomes smaller and smaller as we move seaward. Formulas given in Appendix A are used to compute the vertical co-seismic movements of the sea bottom. They are derived from Okada's (1985, 1992) model, which is valid for finite faults, by taking the limit as the fault length goes to infinity. As the problem is two-dimensional, an obvious consequence is that all the faults considered here are parallel to the coastline, and give rise to tsunamis that hit the coast with normal incidence. Parameters of the seismic sources are listed in table 1. The evolution of the tsunamis can be computed by applying the formulas deduced in the previous section. Figure 4 portrays the initial sea-surface profiles (open triangles) computed by using the four-term expression (3.20) and by determining the set of coefficients c_k $(k = 1, 2, 3, 4)$ that lead to the best fit of the corresponding initial sea-bottom profiles (solid lines) resulting from the application of the dislocation theory. The fit procedure is based on a simple trial and error technique and gives satisfactory results. The coefficients estimated for the four cases are listed in table 2. Note that, though co-seismic displacement profiles decay offshore faster than the curves we compute for tsunami analysis, this does not compromise the value of the results for the purpose of this study.

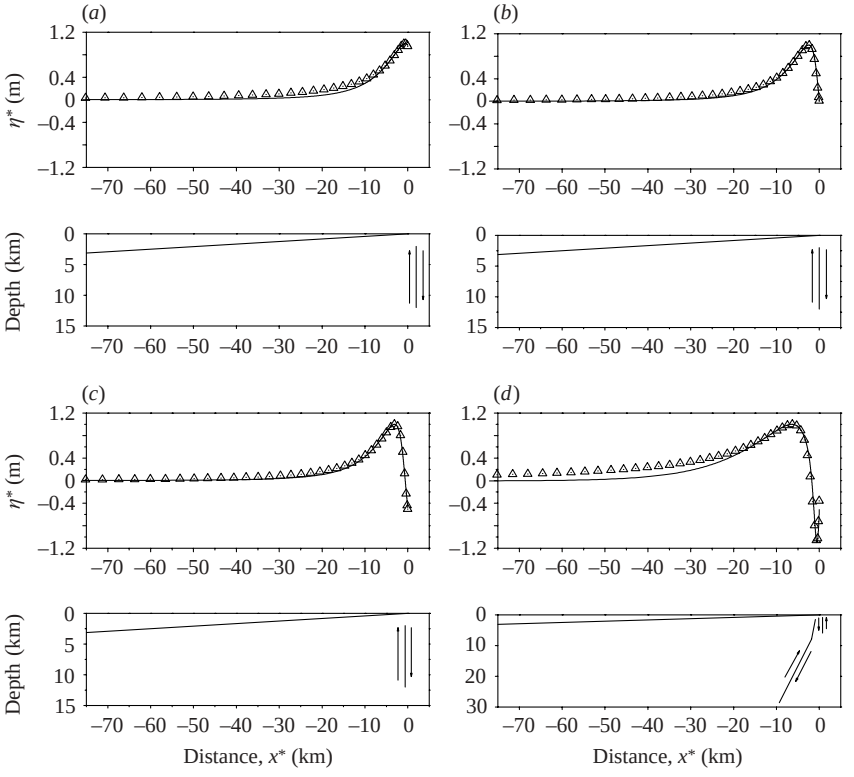

FIGURE 4. Cases 1, 2, 3 and 4 are illustrated in (*a*)–(*d*) respectively. Each has two panels. The upper panel displays the sea-surface vertical displacements induced by coastal earthquakes computed through Okada's model (solid line) compared to the best-fit curves obtained through formula (3.20) (open triangles). The lower panel shows the constant-slope sea bed and the position of the seismic fault. Cases 1–3 are associated with vertical dip–slip faults, that are inland (case 1), beneath the coastline (case 2) and slightly offshore (case 3). Case 4 is associated with a system of faults: a two-segment inverse fault (to the left) formed by fault 1 and fault 2 of table 1, and a small ancillary normal fault (to the right), that is fault 3 of table 1.

	bl_0c_0	bl_0c_1	bl_0c_2	bl_0c_3
Case 1	4.0920	−4.2543	1.1051	0.00035
Case 2	1.9958	13.2683	−31.6044	16.34029
Case 3	1.4797	19.1177	−44.6004	23.49390
Case 4	14.2123	−28.7658	0.5594	13.76120

TABLE 2. Coefficients used in expression (3.20) to compute the initial sea-surface profiles of cases 1–4 illustrated in figures 4–12. The values are multiplied by bl_0, which is the scaling factor used to normalize the water elevation according to the scaling law (3.5). In these examples, $bl_0 = 2000$.

The discussion will be conducted here using the dimensional variables since we believe that this choice helps the reader to grasp better the physics and the correct scale of the phenomena we deal with. Correspondingly, we also adopt realistic values for the parameters l_0 (horizontal scale) and b (bottom slope) of the model: the former is taken to be equal to 50 km, whereas for the latter the value $b = 1/25$ is selected,

since it is typical for the sea depth gradient averaged over a coastal belt 100 km wide in many regions of the world. In this section, we have standardized the initial sea-surface maximum elevation, which we designate η^*_{max}, to the value of 1 m, in order to permit an easier comparison among the various cases. In the rest of the paper, tsunami evolution will be illustrated with the aid of two kinds of plots: water elevation profiles taken at a specified time and time histories of the water elevation and velocity at the coastline. The procedure to compute such curves is simple and is outlined below. In the former case, let us specify the dimensional time t^* at which the profile is desired and a set of values for the dimensionless coordinate $\sigma_j = j\Delta\sigma$ ($j = 0, 1, \ldots, N$) where $\Delta\sigma$ is a step of appropriate size. Then, by virtue of the scaling law (3.6) and of the transformation relation (3.12), a useful iteration scheme can be set up:

$$\lambda_j^{(n)} = 2\left[t^*/T + v\left(\sigma_j, \lambda_j^{(n-1)}\right)\right],$$

where the velocity v is calculated with the aid of equation (3.22). Let us call λ_j the limit of the above sequence. If the initial values to start the procedure are taken as

$$\lambda_0^0 = 0, \tag{4.1}$$

$$\lambda_j^0 = \lambda_{j-1}, \tag{4.2}$$

only a few iteration steps are needed to estimate λ_j. Once λ_j is known, the dimensional water elevation η_j^* and the corresponding coordinate x^* are computed by means of

$$\eta_j^* = bl_0\eta(\sigma_j, \lambda_j), \tag{4.3}$$

$$x_j^* = l_0\left[\eta(\sigma_j, \lambda_j) - \frac{\sigma_j^2}{16}\right]. \tag{4.4}$$

The set of values (η_j^*, x_j^*) is the discrete representation of the water surface profile we seek. By adapting the parameters $\Delta\sigma$ and N we can change the resolution and the length of the profile. In an analogous way, we can proceed to compute the coastline time histories. We consider the set of values $\lambda_j = j\Delta\lambda$ ($j = 0, 1, \ldots, N$) and compute the corresponding dimensionless coastal velocities and elevations $v_{cj} = v_c(\lambda_j)$ and $\eta_{cj} = \eta_c(\lambda_j)$ by means of equations (3.26) and (3.27). Then we can exploit the hodograph transformation (3.12) and the scaling relationships (3.4)–(3.6) to obtain

$$t_j^* = T\left(\frac{\lambda_j}{2} - v_{cj}\right), \tag{4.5}$$

$$\eta_j^* = bl_0\eta_{cj}, \tag{4.6}$$

$$x_j^* = l_0\eta_{cj}. \tag{4.7}$$

The pairs (v_{cj}^*, t_j^*) and (η_{cj}^*, t_j^*) are the discrete dimensional forms of the time histories sought with resolution and length governed by $\Delta\lambda$ and N respectively. The evolution of the tsunami produced by the fault of case 1, with the initial profile portrayed in figure 4(*a*), is shown in figure 5 by means of a series of snapshots taken at various times. It is a mild tsunami with water elevation in the order of 1 m at the coast ($\eta^*_{max} = 1$ m is attained slightly offshore), produced by an earthquake with fault slip larger than 3 m (see table 1). The sea reference level is the unperturbed water level far from the source, which coincides also with the level of the sea as time t^* grows larger. The earthquake dislocation does not change the sea reference level, since a local limited-extent perturbation, like the one produced by the earthquake, cannot have an effect on the level of the entire ocean. But it has the effect of modifying the position of the shoreline permanently. The shore uplift causes the pre-event shoreline to be offset

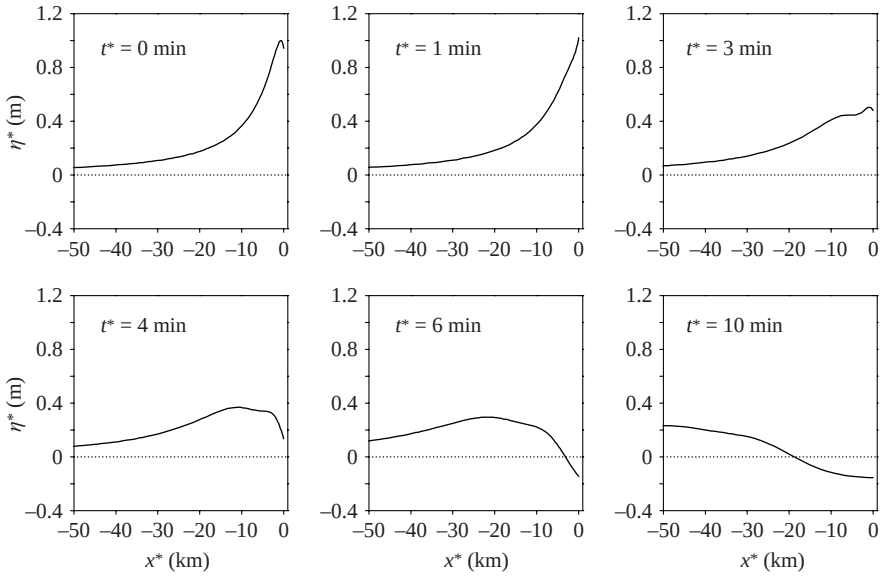

FIGURE 5. Case 1. Water elevation profiles computed at various times.

upward and to take a new position after the end of the tsunami. During the first minute or so, the sea water piles up against the coast and penetrates a little beyond the old shoreline. In the following 5 minutes, it retreats towards the new shoreline, crossing it slightly later. At around 8 minutes, it reversess motion, advancing slowly to the final position. The oscillatory movement of the shoreline is very simple (up–down–up). It moves quite slowly, its velocity almost vanishing around 10 minutes after the earthquake. The shoreline movement and the instantaneous velocity of the water are plotted in figure 6. Case 2 tsunami is depicted in figures 7 and 8. The coastline is not offset by the earthquake, while the sea floor is uplifted. The initial single bulge of the sea surface tends to split into a sequence of two waves: one reflects from the coast before travelling seaward, while the other propagates seaward from the beginning, as can be seen from the series of water elevation profiles computed at different times (figure 7). On the coast only one oscillation is visible, which inundates the shore and retreats in about 5 minutes (figure 8). The process of sea withdrawal beyond the usual shoreline is very slow and mild. Case 3 is a tsunami caused by an undersea fault, causing subsidence of the shore and uplift of the offshore sea floor. The qualitative tsunami evolution is not dissimilar from case 2. Two waves form, one of which reflects from the coast before travelling seaward (figure 9). At the coast, the sea water is seen first to advance beyond the old shoreline and to flood the beach (figure 10). The maximum inundation is reached in about 3 minutes. Then the shoreline retreats, but remains above its old level. Case 4 is the case of coastal subsidence, with the maximum subsidence found some distance offshore and sea-bed uplift at a larger distance from the coast. The initial form of the wave is a crest–trough system with a trough that is truncated and on the coastal side. The sea water profiles are more complex than in previous cases. The crest–trough divides into two systems. The one impacting the coast is reflected and reversed, and then travels seaward following the other (figure 11). The first tsunami manifestation at the coast is the retreat of the shoreline below the old limit, due to the arrival of the wave trough. After that, the sea level begins rising and the incoming crest inundates the beach (figure 12). The following water withdrawal

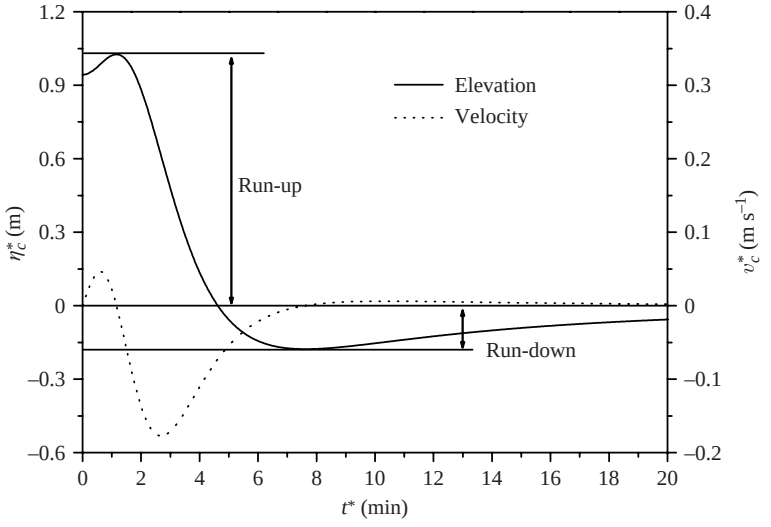

FIGURE 6. Case 1. Elevation η_c^* and velocity v_c^* of the instantaneous shoreline vs. time. Run-up and run-down are referred to the mean sea level, which is not affected by the co-seismic displacement of the Earth's surface. $\eta_c^*(0)$ is the initial elevation of the coastline produced by the earthquake measured from the mean sea level.

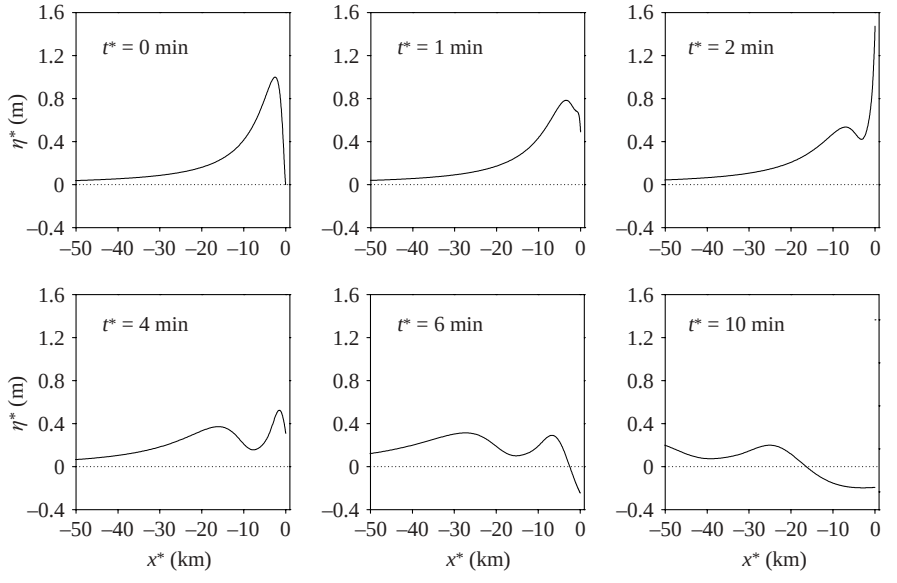

FIGURE 7. Case 2. Water elevation profiles computed at various times.

is moderate and does not go beyond the old level. The impact of the tsunami is accompanied by corresponding water currents with speed exceeding 1 m s^{-1}.

One of the main questions about the interaction of tsunamis with the coast concerns the amplification. If we define R_{up} and R_{down} as the maximum and the minimum elevation at the coast with respect to the sea reference level, and if we call η^*_{min} the minimum elevation of the initial sea-surface profile (in analogy with the quantity η^*_{max}

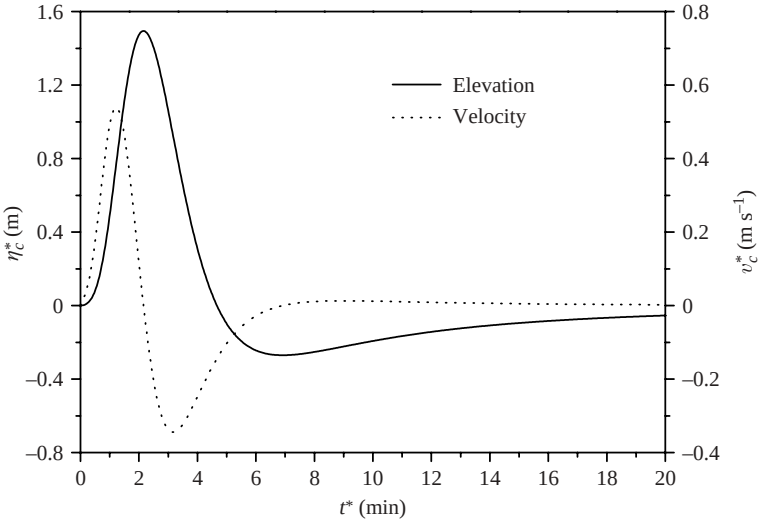

FIGURE 8. Case 2. Elevation η_c^* and velocity v_c^* of the instantaneous shoreline vs. time.

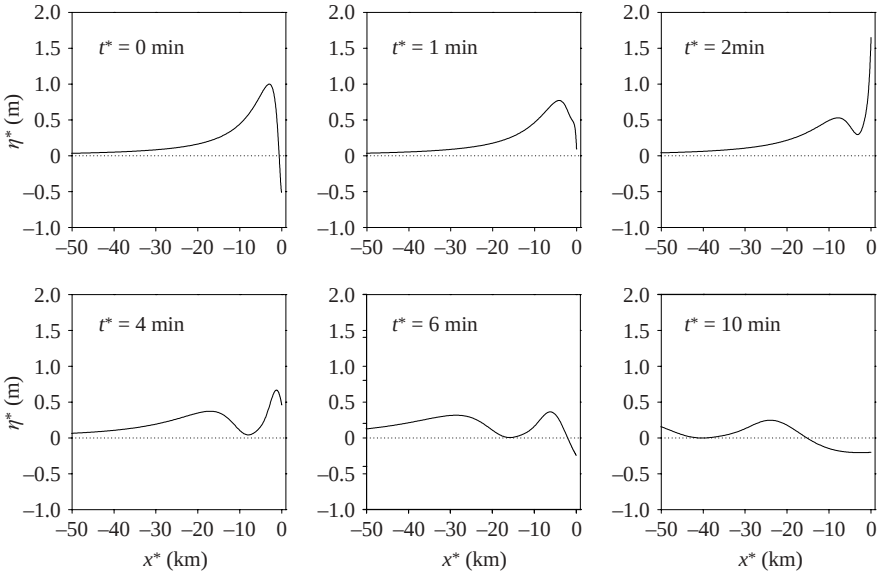

FIGURE 9. Case 3. Water elevation profiles computed at various times.

defined previously), then the amplification factor A may be computed as

$$A = \frac{R_{up} - R_{down}}{\eta^*_{max} - \eta^*_{min}} \tag{4.8}$$

which is the ratio of the maximum vertical excursion of the wave measured at the coast and the initial wave height. A further interesting aspect is the potential flooding by the tsunami, that is the capability of the tsunami to inundate land, which is influenced drastically by the vertical co-seismic displacement of the coast. In our notation, the elevation of the coast at time $t^* = 0$, i.e. $\eta_c^*(0)$, corresponds to the offset caused by the earthquake. It is the vertical position of the old pre-earthquake shoreline. The

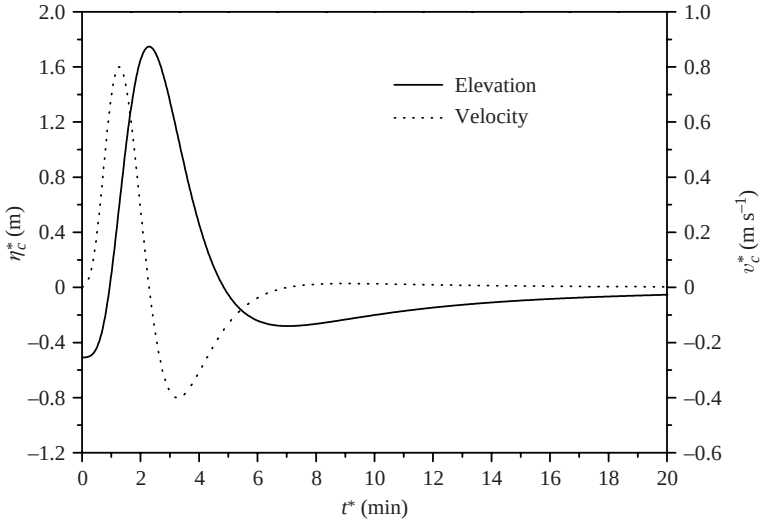

FIGURE 10. Case 3. Elevation η_c^* and velocity v_c^* of the instantaneous shoreline vs. time.

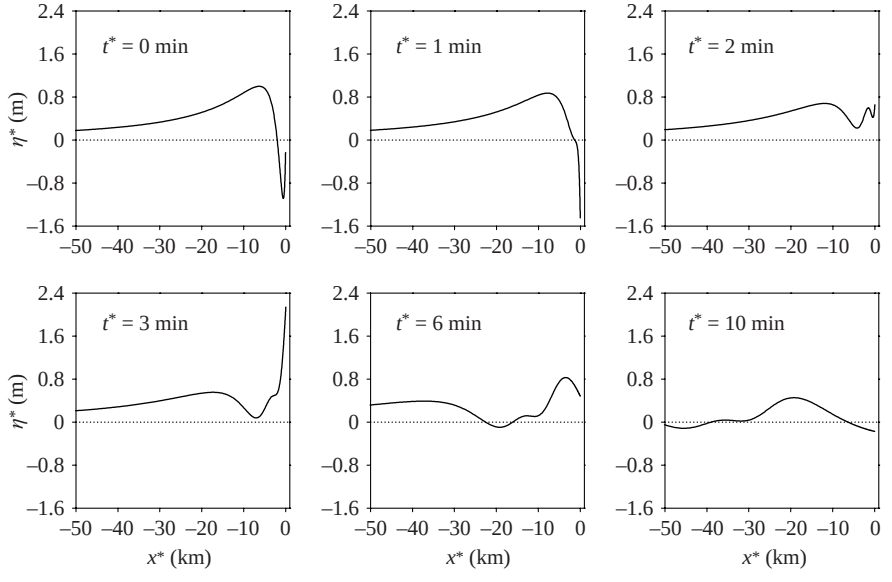

FIGURE 11. Case 4. Water elevation profiles computed at various times.

difference $R_{up} - \eta_c^*(0)$ is the vertical projection of land that is flooded temporarily by waves, and correspondingly the ratio $(R_{up} - \eta_c^*(0))/b$ is the horizontal projection of the inundated land. It is convenient to introduce the flooding factor F_f, which we define here as follows:

$$F_f = \frac{R_{up} - \eta_c^*(0)}{R_{up} - R_{down}}, \tag{4.9}$$

which is in the range [0,1] and is the fraction of the coastal wave height that causes inundation beyond the old shoreline level. Its complement to 1 which we designate

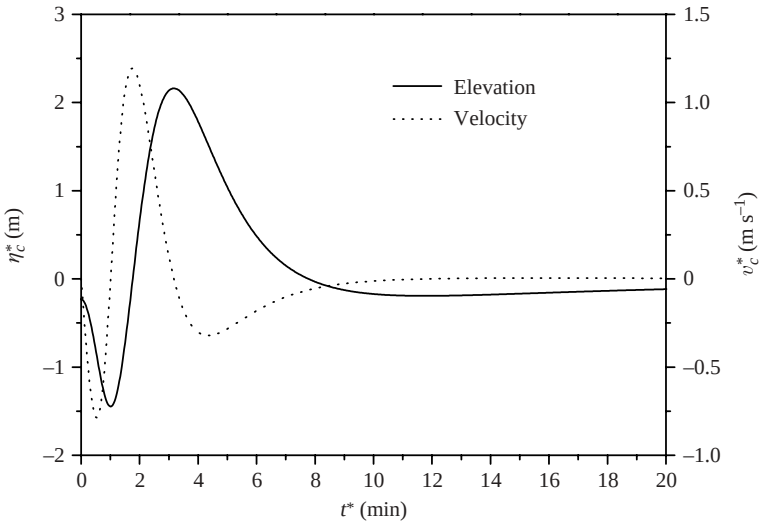

FIGURE 12. Case 4. Elevation η_c^* and velocity v_c^* of the instantaneous shoreline vs. time.

	η^*_{min} (m)	η^*_{max} (m)	$\eta^*_c(0)$ (m)	R_{down} (m)	R_{up} (m)	A	F_f (%)	F_d (%)
Case 1	0.000	1.000	0.943	−0.178	1.026	1.204	6.9	93.1
Case 2	0.000	1.000	0.000	−0.270	1.494	1.764	84.7	15.3
Case 3	−0.509	1.000	−0.509	−0.509	1.748	1.496	100.0	0.0
Case 4	−1.085	1.000	−0.233	−1.477	2.161	1.730	66.4	33.6
Case 4 ($K = 5$)	−5.425	5.000	−1.165	−7.235	10.805	1.730	66.4	33.6
Case 4 ($K = -1$)	−1.000	1.085	0.233	−2.161	1.477	1.730	33.6	66.4
Case 4 ($K = -5$)	−5.000	5.425	1.165	−10.805	7.235	1.730	33.6	66.4

TABLE 3. Water elevation, amplification coefficient A and flooding and drying factors F_f and F_d for the four cases.

as F_d and call the drying factor, is

$$F_d = \frac{\eta_c^*(0) - R_{down}}{R_{up} - R_{down}}. \tag{4.10}$$

It is similarly the fraction of the coastal height quantifying the withdrawal of the sea water from the old coastline and causing the sea floor to appear temporarily dry. Table 3 lists the amplification coefficient A and the flooding and drying factors, F_f and F_d, computed for the four cases treated above. The amplification factor ranges from 1.2 to 1.76, which means that the tsunami at the coast is seen to be slightly larger than offshore. Notice that run-up R_{up} and amplification factors A do not correspond with each other. Case 4 produces the largest R_{up} (2.161 m), but not the largest tsunami-height amplification. The flooding factors differ significantly, since they discriminate between coastal subsidence and coastal uplift: after seismic subsidence, coastlines are much more prone to tsunami flooding, that is to inundation beyond the pre-earthquake shoreline level (cases 3 and 4), than after coastal uplift (case 1).

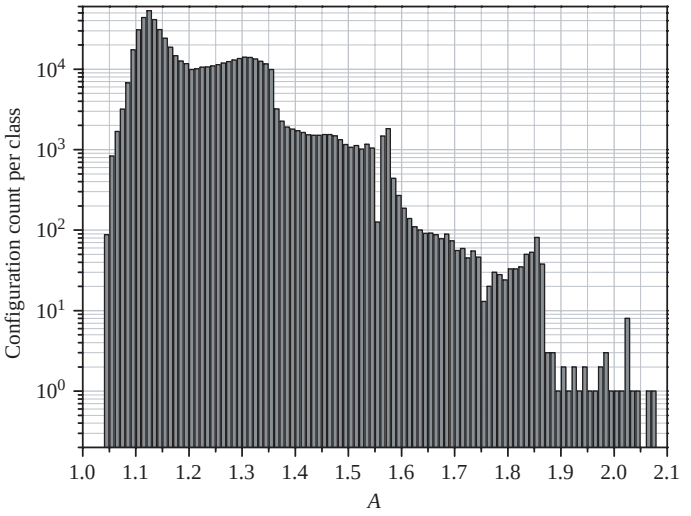

FIGURE 13. Frequency histogram of the amplification factor A. The total number of configurations explored is $N_c = 538\,084$. The class width is 0.1. The amplification factors found range from 1.046 to 2.076.

5. Analysis of the influence of the initial waveform

The analysis of the four cases associated with the seismic sources illustrated in figure 4 has provided interesting results. We found that different initial sea-surface profiles give rise to different amplifications, and is relevant to explore the effect of the initial tsunami waveform in a more systematic way. We restrict ourselves to the class of waveforms that can be obtained by using the four-coefficient expression (3.20), since these can be connected to the co-seismic displacement fields of near-shore crustal faults. We have considered a large number of configurations $[c_0, c_1, c_2, c_3]$ by varying the coefficients, and for each configuration we have computed the initial sea-surface profile and the coastal time history, calculating the amplification factor A as well as all other relevant coefficients (R_{up}, R_{down}, etc.). Here we present the results of the analysis of $N_c = 538\,084$ configurations. To aid comparison, all configurations have the properties of producing normalized profiles, with unitary initial wave height, that is $\eta^*_{max} - \eta^*_{min} = 1$ m, and of having a prevailing positive wave, that is $\eta^*_{max} > |\eta^*_{min}|$. Moreover, the numerical process that generates the ensemble of configurations checks easily that no configuration is repeated.

The histogram of the amplification factors that we found is plotted in figure 13. The frequency graph has no probability significance, since there is no occurrence probability value attached to each configuration. Nonetheless it is interesting to note that the distribution of the computed amplification coefficient has a mean value of 1.208 and standard deviation of 0.106, while the mode is around 1.25. It is more interesting to take account of the extremes of this distribution: the minimum and maximum amplifications are 1.046 and 2.076 respectively. Figure 14 shows 12 configurations selected from all N_c: we selected the ones associated with the maximum and the minimum amplification coefficients A together with a sample of ten configurations corresponding to intermediate amplifications from 1.1 to 2.0, regularly spaced ($\Delta A = 0.1$). Figure 15 shows the corresponding coastal time histories. The analysis of figure 14 enables us to deduce an important correlation between the waveform and the wave height amplification at the coast. The simplest waveforms

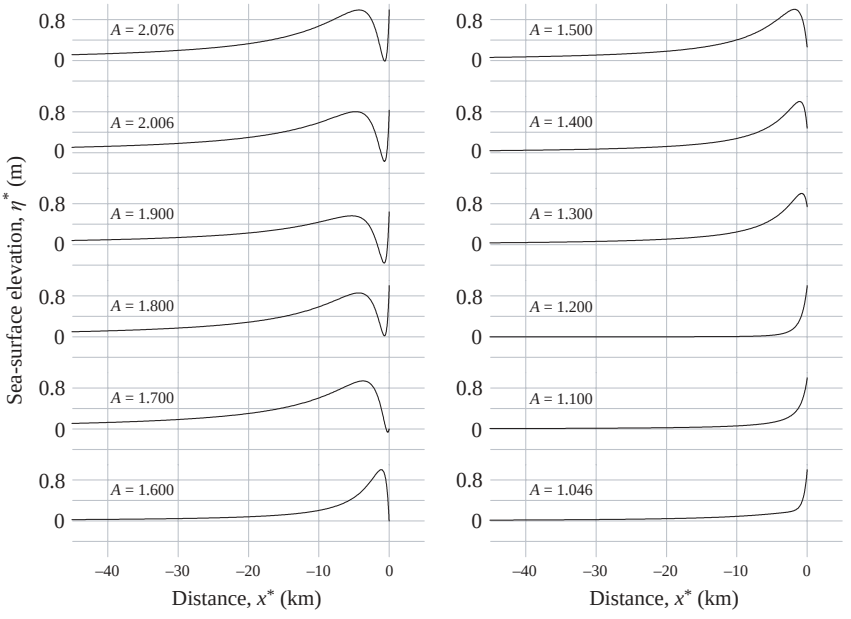

FIGURE 14. Initial sea-surface profiles selected out of the ensemble of N_c configurations: they correspond to the maximum and minimum values of the amplification coefficients found as well as to intermediate values at 0.1 intervals. Note that, since no configuration giving $A = 2.0$ was found in the ensemble, we selected the configuration associated with the next value ($A = 2.006$).

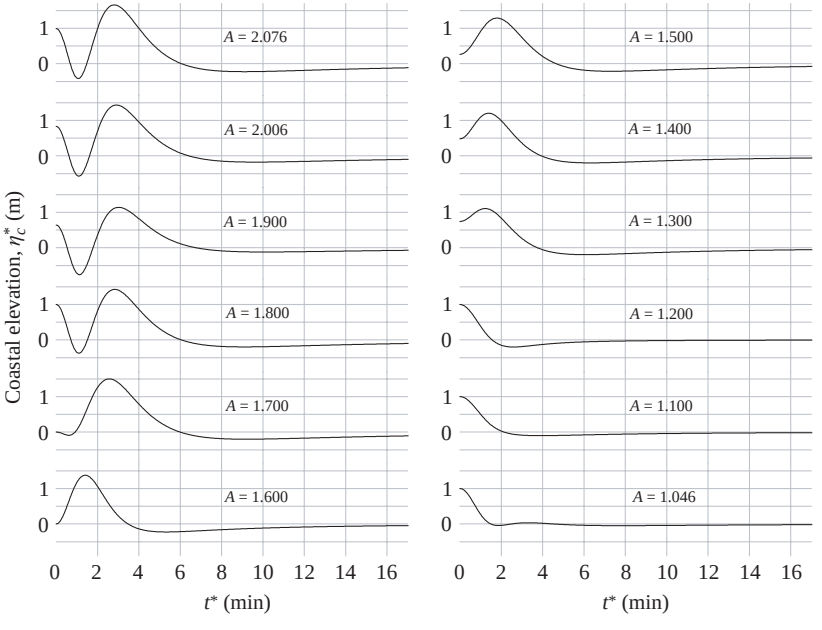

FIGURE 15. Time histories of the shoreline movement for the same selection of configurations as figure 14.

with the highest uplift at the coastline are the ones that are least amplified (A around 1–1.2). In these cases the shoreline moves gradually from the old to the new position (sea retreat) with some small overshooting at most. For profiles where in the seaward

direction the water elevation first increases up to a maximum value and then decreases down to the unperturbed level, the tsunami amplification increases further. This seems to go in parallel with the increase of the difference between the wave maximum level offshore η^*_{max} and the coastal elevation $\eta^*_c(0)$, leading to coefficients between 1.3 and 1.6. Profiles exhibiting one minimum (closer to the coast) and one maximum (further from the coast) water level have even larger amplifications that grow together with the difference $\eta^*_c(0) - \eta^*_{min}$ and are in the highest range 1.7–2.076. Cases 1–4 that we have discussed in the previous section can be easily recognised to fall in one of the above categories. It is also quite useful to observe that all the above profiles can be roughly related to surface vertical displacements of seismic faults that are in the near-shore belt, and that the amplification coefficients clearly seem to grow as the fault position moves from inland to offshore, which is a very relevant result.

6. Analysis of the influence of the wave amplitude

The waveforms that we considered in previous sections were normalized either with respect to η^*_{max} (cases 1–4) or with respect to the tsunami height $\eta^*_{max} - \eta^*_{min}$. The question arises whether the conclusions we drew on the amplification coefficients and the flooding and drying factors can also be applied when the amplitude or height of the initial wave is arbitrary. Here we prove that the results obtained previously are perfectly applicable within the range of amplitudes that can reasonably be expected for tsunamis of seismic origin. To this end, let us assume first that a given profile $bl_0\eta(\boldsymbol{c}|\sigma, \lambda = 0)$, computed through the four-coefficient expression (3.20), represents the initial sea-surface displacement $\eta^*(x^*, t^* = 0)$ caused by an earthquake with a given fault slip. In the above notation we have put in an explicit form the dependence of the profile on the configuration vector $\boldsymbol{c}$ formed by the set of four selected coefficients $[c_0, c_1, c_2, c_3]$. After taking into account relation (3.25) and scaling laws (3.4) and (3.5), we can write the following equations:

$$\eta^*(x^*, t^* = 0) = bl_0\eta(\boldsymbol{c}|\sigma, \lambda = 0), \tag{6.1a}$$

$$x^* = \frac{\eta^*(x^*, t^* = 0)}{b} - \frac{l_0\sigma^2}{16}. \tag{6.1b}$$

It may be recalled that the space coordinate x^* is measured from the position of the post-earthquake coastline. If we introduce the space coordinate ξ^* referred to the pre-earthquake shoreline location, then it is straightforward to write the relation between the two reference frames:

$$x^* = \xi^* - l_0\eta_c(\boldsymbol{c}) \tag{6.2}$$

where $\eta_c(\boldsymbol{c}) = \eta(\boldsymbol{c}|\sigma = 0, \lambda = 0)$, and $l_0\eta_c(\boldsymbol{c})$ is the co-seismic horizontal offset of the coastline. Formally $\eta^*(x^*, t^* = 0)$ differs from $\eta^*(\xi^*, t^* = 0)$ and we can use the Taylor expansion truncated to the first order to write

$$\eta^*(x^*, t^* = 0) = \eta^*(\xi^*, t^* = 0) - b\eta_c(\boldsymbol{c})\frac{\partial\eta^*(\xi^*, t^* = 0)}{\partial\xi^*}.$$

If we consider orders of magnitude that are appropriate for the initial waveforms of the tsunamis, that is

$$o(\eta^*(x^*, t^* = 0)) = 1\text{–}10\,\text{m} \quad \text{initial elevation in the post-earthquake reference frame,}$$

$$o(\eta^*(\xi^*, t^* = 0)) = 1\text{–}10\,\text{m} \quad \text{initial elevation in the pre-earthquake reference frame,}$$

$$o(b\eta_c(\boldsymbol{c})) = 1\text{–}100\,\text{m} \quad \text{horizontal permanent displacement of the shoreline,}$$

$$o\left(\frac{\partial \eta^*(\xi^*, t^*=0)}{\partial \xi^*}\right) = 10^{-4}\text{–}10^{-3} \quad \text{gradient of the initial tsunami waveform,}$$

we may easily conclude that the following approximation holds:

$$\eta^*(x^*, t^*=0) \approx \eta^*(\xi^*, t^*=0). \tag{6.3}$$

Given the above premises, let us now consider the effect of a seismic source possessing exactly the same characteristics as a given fault, except for the fault slip, which is supposed to be multiplied by the factor K. Owing to the linear dependence of the source dislocation and co-seismic displacements upon the slip magnitude, we conclude that the sea-surface profile associated with this new case is $K\eta^*(\xi^*, t^*=0)$, or, by virtue of the approximation (6.3), $K\eta^*(x^*, t^*=0)$. Now the problem is that of finding the configuration vector $\boldsymbol{c}'$ that is the most suitable to represent this profile. To this end, we can set up a system of equations analogous to (6.1a, b), i.e.

$$K\eta^*(x'^*, t^*=0) = bl_0\eta(\boldsymbol{c}'|\sigma, \lambda=0), \tag{6.4a}$$

$$x'^* = \frac{K\eta^*(x'^*, t^*=0)}{b} - \frac{l_0\sigma^2}{16}, \tag{6.4b}$$

where we have introduced the horizontal variable x'^* for reasons that will be clarified soon. Expression (3.20) being a linear function of the configuration vector, equation (6.4a) is satisfied if and only if $\boldsymbol{c}' = K\boldsymbol{c}$, since

$$\eta(\boldsymbol{c}' = K\boldsymbol{c}|\sigma, \lambda=0) = K\eta(\boldsymbol{c}|\sigma, \lambda=0).$$

On the other hand, the coordinate transformation (6.4b) is not linear and if a pair of (x^*, σ) is a solution of (6.1b), it cannot also satisfy equation (6.4b). Let us examine the property of the solution corresponding to the configuration $\boldsymbol{c}' = K\boldsymbol{c}$. Equation (6.4$a$) tells us that this solution has elevation exactly a factor K larger than η^*, as desired, but equation (6.4b) states that it is attained not at x^*, as required, but at the horizontal position x'^* that is related to x^* by

$$x'^* - x^* = (K-1)l_0\eta(\boldsymbol{c}|\sigma, \lambda=0). \tag{6.5}$$

However, the shift (6.5) has size comparable with shift (6.2), and correspondingly, it can be considered negligible, which leads us to the conclusion that the configuration $\boldsymbol{c}' = K\boldsymbol{c}$ provides an acceptable solution to the problem. We notice that while shift (6.2) is uniform, i.e. independent of the position, since it corresponds to the constant offset of two reference frames, the shift (6.5) depends on the elevation $\eta(\boldsymbol{c}|\sigma, \lambda=0)$, which has the effect of changing the waveform slightly. If $K > 1$, positive maxima of the amplified tsunami $\eta(K\boldsymbol{c}|\sigma, \lambda=0)$ are shifted landward, whereas zeros do not change position and negative minima are shifted seaward, with the net effect that the initial waveform of $\eta(K\boldsymbol{c}|\sigma, \lambda=0)$ is steeper than the one associated with $\eta(\boldsymbol{c}|\sigma, \lambda=0)$. However, this change is irrelevant as long as we consider quantitative values that are appropriate for real tsunamis of seismic origin.

The above analysis holds even when the factor K is negative. Using negative factors means interchanging positive and negative water elevations and corresponds to inverting the sign of the seismic slip on the faults. Thrust faults become normal faults, and zones of subsidence are replaced by uplift and vice versa. Figure 16 shows the time histories of the shoreline elevation computed for case 4 discussed in § 4 and of three more tsunamis obtained by using positive and negative values of multiplying

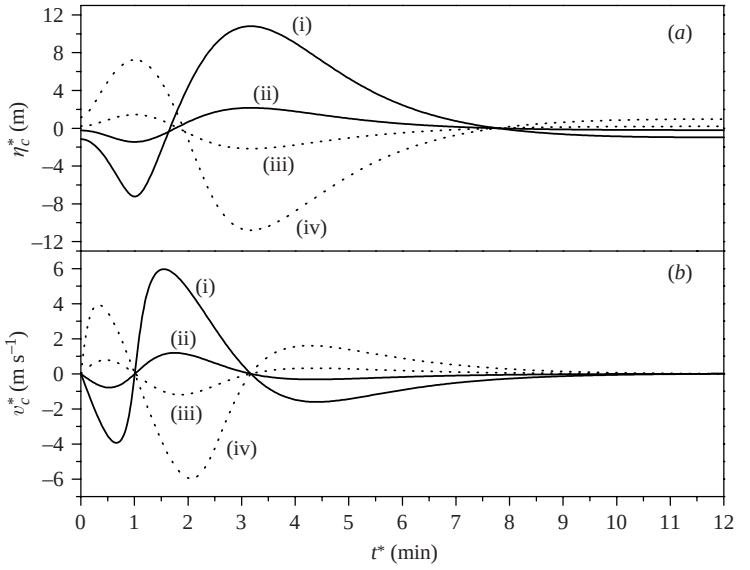

FIGURE 16. (*a*) Coastal water elevation and (*b*) coastal velocity vs. time for four tsunamis, with case 4 (see figure 4*d*) selected as the reference case. In this graph it is plotted as (ii). The others are obtained by using the multiplying factors $K = 5$ (i), $K = -1$ (iii) and $K = -5$ (iv) to compute the configuration vector. Observe that all velocity curves intersect exactly as the velocity vanishes, which means that all tsunamis take exactly the same time to reach the run-up and the run-down heights. The curves of each panel are similar, but they do not have exactly the same shape, since the problem is nonlinear. Nonlinear terms deform the velocity curves remarkably: oscillations of large-amplitude waves tend to be asymmetric.

factors. As regards the behaviour of the amplified tsunami at the coast, it is worth observing that, due to the nonlinearity of the set of expressions (3.26), (3.27) and (3.12), the following inequalities hold:

$$v_c^*(K\boldsymbol{c}|t^*) \neq K\, v_c(\boldsymbol{c}|t^*)$$

and

$$\eta_c^*(K\boldsymbol{c}|t^*) \neq K\, \eta_c(\boldsymbol{c}|t^*).$$

But, if attention is focused on run-ups and run-downs, which correspond exactly to turning points of the shoreline motion and hence satisfy the condition of vanishing velocity, then the following relations can be written:

$$R_{up}(K\boldsymbol{c}) = \max\{bl_0\eta_c(K\boldsymbol{c}|\lambda)\} = \max\{Kbl_0\eta_c(\boldsymbol{c}|\lambda)\} = K\,R_{up}(\boldsymbol{c}), \tag{6.6}$$

$$R_{down}(K\boldsymbol{c}) = \min\{bl_0\eta_c(K\boldsymbol{c}|\lambda)\} = \min\{Kbl_0\eta_c(\boldsymbol{c}|\lambda)\} = K\,R_{down}(\boldsymbol{c}). \tag{6.7}$$

Further, we stress that all tsunamis differing each other only by an amplifying factor reach their maximum inundation and retreat at the coast at the same time. This is the trivial consequence of the hodograph law (3.12). Indeed, both functions $\eta_c(K\boldsymbol{c}|\lambda)$ and $\eta_c(\boldsymbol{c}|\lambda)$ attain their maximum and minimum in correspondence with the same respective value of λ_{max} and λ_{min} which do not depend on K. Further, the transformation law

$$t^* = T\frac{\lambda}{2} - \frac{T}{v_0}v_c(\lambda),$$

though in general depending on K through $v_c(\lambda)$, reduces to

$$t^*_{max} = T\frac{\lambda_{max}}{2}, \quad t^*_{min} = T\frac{\lambda_{min}}{2}$$

for all possible K, as we wanted to prove.

Since all the relevant quantities that appear in the definition of the amplification coefficient A given by the ratio (4.8) are proportional to the multiplying factor K, it follows that A is independent of K, which justifies *a posteriori* the use we made of normalized tsunamis in the previous sections. Further, since using negative values for K exchanges the roles of minima and maxima both on the profiles ($\eta_{max} \rightarrow \eta_{min}$) and on the coastal time histories ($R_{up} \rightarrow R_{down}$), it can immediately be seen that the flooding and drying factors also exchange each other ($F_f \rightarrow F_d$). The last rows of table 3 illustrate the effect of applying multiplying factors to the tsunami of case 4, complementing the results shown in figure 16.

The observed independence of the amplification coefficient A of the factor K implies that one obtains the same value of A for very large as well as for very small waves, provided that they possess the same waveform. Hence, since small waves can be treated by means of the linear theory, it follows that the linear theory can be conveniently used to compute wave amplifications, which is a feature that was already pointed out in the literature by other authors such as Carrier (1971), Synolakis (1987), Synolakis (1991), Pelinovsky & Mazova (1992), and Carrier *et al.* (2003).

7. Analysis of the influence of the ocean bottom slope

In order to examine the effect of the sea-floor slope on the tsunami evolution, we can follow the same kind of analysis we performed in the section above. Let us suppose that the same earthquake causes the displacement of the sea bottom in two oceans having different bottom slopes b and b'. If we denote by $\eta^*(x^*, t^* = 0)$ the initial sea-surface profile in the post-earthquake reference frame, and neglect the horizontal shift between the pre-earthquake and post-earthquake coordinates by virtue of the same approximation (6.3), we can write the following sequence of equations:

$$\eta^*(x^*, t^* = 0) = bl_0\eta(\boldsymbol{c}|\sigma, \lambda = 0) = b'l_0\eta(\boldsymbol{c}'|\sigma, \lambda = 0),$$

from which we deduce the following relation between the configuration vectors of the two geometries:

$$\boldsymbol{c}' = \frac{b}{b'}\boldsymbol{c}.$$

The link between the run-ups and the draw-downs associated with the two ocean beaches can be inferred accordingly as

$$R'_{up} = b' \max\{\eta_c(\boldsymbol{c}'|\lambda)\} = b' \max\left\{\frac{b}{b'}\eta_c(\boldsymbol{c}|\lambda)\right\} = b \max\{\eta_c(\boldsymbol{c}|\lambda)\} = R_{up},$$

$$R'_{down} = b' \min\{\eta_c(\boldsymbol{c}'|\lambda)\} = b' \min\left\{\frac{b}{b'}\eta_c(\boldsymbol{c}|\lambda)\right\} = b \min\{\eta_c(\boldsymbol{c}|\lambda)\} = R_{down}.$$

This shows that the extreme water elevations at the coast do not depend upon the sea-floor slope, given the same initial sea-surface profile. The transformation law (3.12) as well as the normalizing laws for the time and the velocity (3.6) and (3.3) show however that both the time scale and velocity scale depend on the parameter b. When b is small, then the oscillation takes more time to complete and the wave

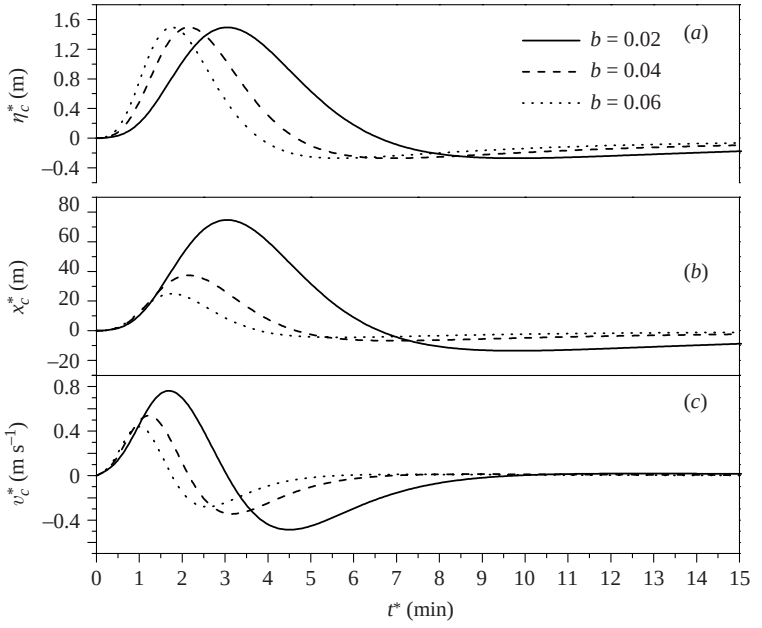

FIGURE 17. Dependence on the bottom slope b. Time histories of (a) the coastal water elevation η_c^*, (b) sea penetration x_c^* and (c) water velocity v_c^*. Run-ups and run-downs are unaffected by the slope (a). The smaller the slope, the shallower is the ocean for a given distance from the shore, and, as regards the tsunami, (i) the slower is the oscillation and the larger is the wave period, (ii) the larger is the horizontal velocity of the water (c), (iii) the larger are the water inland penetration and the sea retreat offshore (b).

period is longer. On the other hand, the horizontal velocity grows and the tsunami advances and retreats by a longer path. Figure 17 shows plots of coastal time histories of the shoreline movement, computed for the reference case 2 and for three different values of the slope ($b = 0.02$, $b = 0.04$ and $b = 0.06$), the intermediate value being the one considered in all previous examples. As far as the amplification coefficient is concerned, our conclusion is that there is no influence of the slope b on A, and this conclusion is also true for both the flooding and drying factors F_f and F_d.

8. Analysis of wave breaking

Wave breaking for long waves evolving on a constant slope and governed by equations (3.13) is studied by considering the Jacobian of the hodograph transformation (3.9)–(3.12), namely $\partial(x, t)/\partial(\sigma, \lambda)$, that can be put in the following form (Spielvogel 1975):

$$\frac{\partial(x,t)}{\partial(\sigma,\lambda)} = \frac{\sigma}{4}\gamma(\sigma,\lambda) \quad \gamma(\sigma,\lambda) = \left[(v_\sigma)^2 - \left(\tfrac{1}{2} - v_\lambda\right)^2\right]. \tag{8.1}$$

Vanishing of the Jacobian occurs either at $\sigma = 0$, that is at the moving shoreline, for all the solutions of the problem, or when $\gamma(\sigma, \lambda) = 0$, which is a condition that not all waves match and that can be taken as the mathematical expression for the condition of wave breaking. For small-amplitude waves it may be proven that $\gamma(\sigma, \lambda) \approx -1/4$, since both derivatives of the velocity have absolute value small compared to $1/2$, and therefore these waves evolve regularly in the (x, t)-space without breaking. Given a non-breaking solution $v(\sigma, \lambda)$ of the linear equation (3.13) for which the function

$\gamma(\sigma, \lambda)$ is non-zero in the entire domain (σ, λ), it is of interest to pose the question whether, multiplying it by a coefficient k, one obtains a wave that breaks during its evolution. In this case the breaking condition can be written as

$$(kv_\sigma)^2 - \left(\tfrac{1}{2} - kv_\lambda\right)^2 = 0 \tag{8.2}$$

which is a quadratic equation in the unknown parameter k admitting the following two real roots:

$$k_1(\sigma, \lambda) = \frac{1}{2(v_\lambda - v_\sigma)}, \quad k_2(\sigma, \lambda) = \frac{1}{2(v_\lambda + v_\sigma)}. \tag{8.3}$$

Both roots depend on the variables σ and λ, since the velocity derivatives do. Further, there is no loss of generality in assuming that, for ordinarily evolving non-breaking waves, the sum and the difference of the velocity derivatives in the denominators of (8.3), and consequently also k_1 and k_2, can take positive and negative values over the (σ, λ)-domain. Under this hypothesis, the value of the coefficient given by

$$K_{b,1} = \frac{1}{2\max(v_\lambda \pm v_\sigma)} > 0, \tag{8.4a}$$

where the maximum is sought over the entire domain $(\sigma \geqslant 0, \lambda \geqslant 0)$, is the minimum value that transforms the non-breaking wave $v(\sigma, \lambda)$ into a breaking wave. On the other hand, it is straightforward to see that the value

$$K_{b,2} = -\frac{1}{2\min(v_\lambda \pm v_\sigma)} > 0, \tag{8.4b}$$

is the minimum coefficient leading $-v(\sigma, \lambda)$ to a breaking condition. For this reason, here $K_{b,1}$ and $K_{b,2}$ are designated as the breaking factors, and can be interpreted as indicators of whether the given wave will break. Any solutions of the kind $\alpha_1 v(\sigma, \lambda)$ with $0 < \alpha_1 < K_{b,1}$ or of the kind $-\alpha_2 v(\sigma, \lambda)$ with $0 < \alpha_2 < K_{b,2}$ correspond to non-breaking waves. Also, the higher $K_{b,1}$ and $K_{b,2}$ are, the further the respective waves $v(\sigma, \lambda)$ and $-v(\sigma, \lambda)$ are from breaking conditions. Notice that the waves $v(\sigma, \lambda)$ and $-v(\sigma, \lambda)$, which have the same initial height and the same amplification factor (see § 6), have in general different breaking factors.

The above analysis can be applied to all the waves that have been treated in the previous sections of this paper that actually represent non-breaking waves. Moreover, it is remarked that all these waves satisfy the conditions that $v_\sigma(\sigma, \lambda = 0) = 0$ (coming from the requirement (3.15) that the initial velocity is zero) and that $v_\sigma(\sigma = 0, \lambda) = 0$ (the velocity being a function of σ^2, according to formula (3.22)). Hence, if the search for K_b is restricted to the axis $\lambda = 0$ and to the axis $\sigma = 0$, forming together the boundary of the domain (σ, λ), then the expressions (8.4a, b) simplify to

$$K^*_{b,1} = \frac{1}{2\max v_\lambda}, \quad K^*_{b,2} = -\frac{1}{2\min v_\lambda}, \tag{8.5}$$

where $K^*_{b,1} \geqslant K_{b,1}$ and $K^*_{b,2} \geqslant K_{b,2}$ are overestimates of the breaking factors. Computing $K^*_{b,1}$ and $K^*_{b,2}$ is much quicker than finding $K_{b,1}$ and $K_{b,2}$, and can provide equally useful information.

It is worth observing that conditions (8.5) correspond to imposing that the derivatives of the solution diverge in the space–time domain. In fact, it is easy to show that for the wave $k\eta(\sigma, \lambda)$ the space derivative of the dimensional elevation

η^* at the initial time $t^* = 0$ (corresponding to $\lambda = 0$) can be put in the form

$$\eta^*_{x^*} = \frac{bkv_\lambda}{kv_\lambda - 1/2}. \tag{8.6}$$

The condition that $kv_\lambda < 1/2$ gives the result that

$$\min(\eta^*_{x^*}) = b \max\left(\frac{kv_\lambda}{kv_\lambda - 1/2}\right),$$

whence it is seen that $\eta^*_{x^*} \to -\infty$ as $\max(kv_\lambda) \to 1/2$, or equivalently as $k \to K^*_{b,1}$. Therefore, it can be stated that the condition of breaking is reached as the initial wave slope in the shoreward transition from a crest to the next trough tends to become vertical. Analogously, at the shoreline (corresponding to $\sigma = 0$), the time derivative of the velocity for the wave $kv(\sigma, \lambda)$ can be written as

$$v^*_{t^*} = \frac{bgkv_\lambda}{1/2 - kv_\lambda}. \tag{8.7}$$

Hence

$$\max(v^*_{t^*}) = bg \max\left(\frac{kv_\lambda}{1/2 - kv_\lambda}\right),$$

and one infers that $v^*_{t^*} \to \infty$ as $\max(kv_\lambda) \to 1/2$, or equivalently as $k \to K^*_{b,1}$. In conclusion, the breaking condition implies that the wave acceleration grows larger and larger, which was already noted by Pelinovsky & Mazova (1992).

We focus here on the set of N_c solutions that were introduced in § 5 where the effect of the initial waveform on the wave evolution was studied. By applying the above analysis to these non-breaking waves, we find the corresponding set of $K^*_{b,1}$ and of $K^*_{b,2}$, which, for simplicity, hereafter will be denoted only as K^*_b. The derivative v_λ, which is needed to compute K^*_b, has the analytical expression given in Appendix B. However, it is observed that on the axis $\lambda = 0$ it is given by the formula (3.21), and at the shoreline it can be conveniently calculated through the numerical approximation $(v_c(\lambda + \Delta\lambda) - v_c(\lambda - \Delta\lambda))/2\Delta\lambda$, which makes use of the equation (3.22). At the origin point, the following equation $v_\lambda(0, 0) = f(0)$ holds:

$$v_\lambda(0, 0) = -8 \sum_{k=0}^{3} \left(\tfrac{3}{2} + k\right) c_k.$$

Notice that since the N_c waves have initial unit height $\eta^*_{max} - \eta^*_{min}$ (in metres), the factor K^*_b can also be interpreted as the initial wave height (in metres) of the minimum-size breaking tsunami. We obtain as many as $2N_c$ values of breaking factors. The results can be illustrated by means of the figures 18 and 19. The computed values of K^*_b vs. the corresponding amplification factor are plotted in figure 18. In order to make the graph more readable, the range of amplification factors has been divided into 52 classes (in the range [1.04, 2.08] with width $\Delta A = 0.02$) and for each class the minimum, the maximum and the mean value of K^*_b, here denoted respectively as $K^*_{b,min}$, $K^*_{b,max}$ and $K^*_{b,ave}$, have been plotted. The first remarks concern the $K^*_{b,min}$ curve, where we see that $K^*_{b,min}$ ranges from about 19 to less than 9 and has a descending trend as the amplification factor increases. This means that none of the waves considered here is expected to break if the initial height is less than 8–9 m, and further, that the simplest waveforms (namely those with a monotonic initial elevation profile, which may be associated with seismic sources with their epicentre on land and are characterized by amplification factors close to 1) are not expected

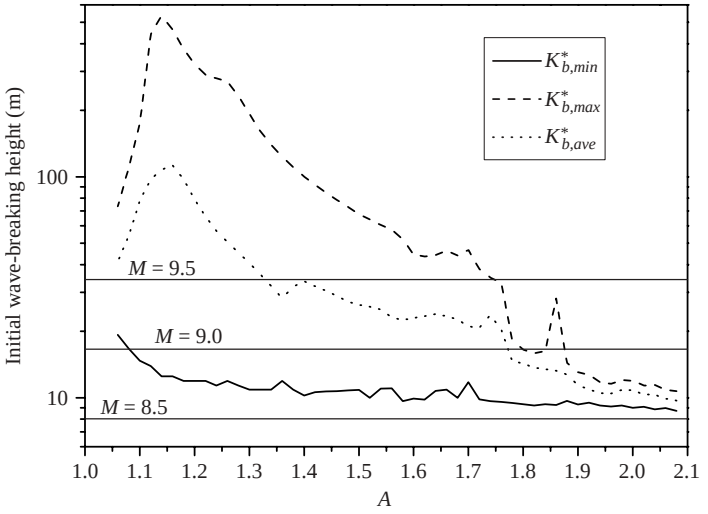

FIGURE 18. Breaking factors vs. the amplification factor computed for all $N_c = 538\,084$ solutions considered in previous analyses. For graphical reasons, the N_c solutions are grouped into 52 classes of amplification factors. $K^*_{b,min}$, $K^*_{b,max}$ and $K^*_{b,ave}$ are the lowest, the largest and the mean value of K^*_b in each class. Since the initial wave height of the N_c solutions is 1 m, the breaking factors can be taken as the minimum initial wave height (in m) that leads to a breaking wave. The horizontal lines are the Earth's surface co-seismic displacements computed through the empirical law obtained by Wells & Coppersmith (1994) as a function of the moment magnitude, and can be taken as reference values for the sea-floor dislocation that can be expected from the largest earthquakes. It can be seen that tsunamis generated by near-shore earthquakes of magnitude $M = 8.5$ or less do not break.

to break even when the initial tsunami height is around 19 m. From figure 18 we can furthermore observe that the computed breaking factors vary over a significantly large range going approximately from less than 9 to more than 500. Such a variability is very large even for solutions having the same amplitude factor, and that, according to our finding in § 5, possess initial elevation profiles falling in the same waveform category and are expected to evolve similarly. Figure 19 is used to illustrate the point. We select four solutions out of the N_c set with the same amplification factor $A = 1.60$, but with different breaking factors K^*_b that are between 13.6 and 28.2. Their profiles are plotted in figure (*a*) and may be associated with an earthquake having its epicentre roughly corresponding with the shoreline. The corresponding solutions in the space (σ, λ) are then multiplied by the smallest breaking factor, i.e. by 13.6. This produces four more solutions with initial wave height equal to 13.6 m, one of which satisfies the breaking condition, while the others do not. In figure 19(*b*, *c*) the initial profiles and the corresponding velocity of the shoreline are given, which shows that the breaking wave exhibits a profile with a vertical slope at the shoreline and a velocity time history $v_c(t^*)$ with a vertical time derivative at the time $t^* = 0$. Observe that this critical situation is very confined in space and time, suggesting that breaking is more influenced by local details of the waveform than by general features, and that small-scale characteristics are more relevant than large-scale ones. The other curves represent non-breaking waves: one of these (having $K^*_b = 14.5$) is close to the breaking condition, while the others are still far from it and will break only in correspondence with larger initial heights.

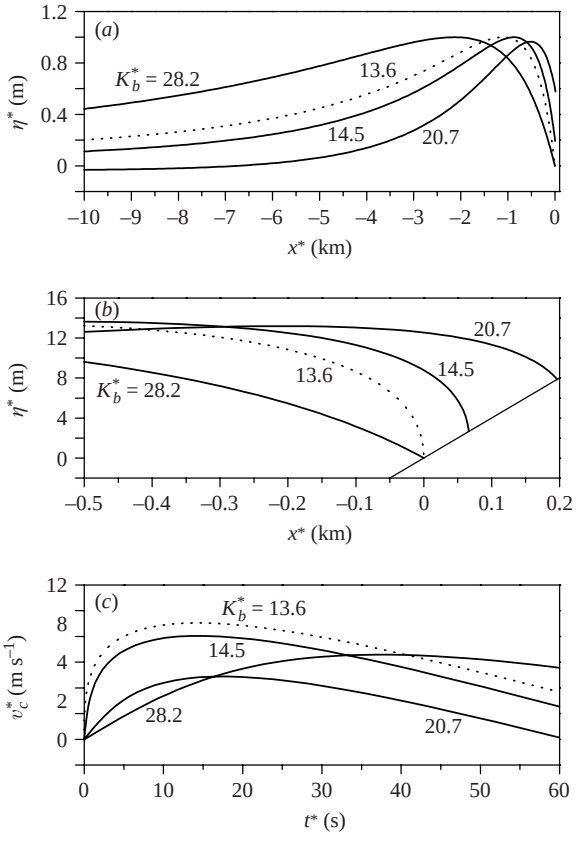

FIGURE 19. (*a*) Profiles of four waves having unit initial height and amplification factor $A = 1.6$, but quite different breaking factors K_b^*; the smallest is 13.6. (*b*) Profiles obtained from those of (*a*) after multiplication by 13.6. (*c*) Time histories of the multiplied waves. Note that multiplication is performed in the space (σ, λ).

9. Conclusions

The analysis that has been performed in this work enabled us to find important results on the characteristics of tsunamis induced by seismic dislocations in near-shore regions, though we have used an idealized bathymetry for the ocean, namely a constant-slope sea floor. The most relevant result concerns the expected amplification of the tsunami at the coast. We have found that the four-coefficient expression (3.20) can be used to provide initial sea-surface profiles that may be related to co-seismic displacements induced by seismic faults. By taking into account a very large number of such profiles (more than 5×10^5) we have found that the amplification coefficient A ranges from 1.046 to 2.076. We cannot rule out that if we sample the four-coefficient initial configuration space differently, we can enlarge the range, but we are confident that the possible extension is very minor. Examining the waveforms, we have found a relation between the amplification coefficient and the number of waves of the initial profiles, that, and this is very interesting, can also be related to the distance of the seismic fault from the coastline. An inner fault, that is a fault inland, produces a sea-surface profile that increases (decreases) monotonically from offshore landward, with the maximum displacement at the coast, and this profile is found to be the least prone to amplification: the tsunami height practically does not change ($A \approx 1$). Moving the

fault toward the sea has the effect of moving the maximum displacement seaward, and, when the source is near-shore but under the sea, the initial profile shows a crest–trough system corresponding to regions of sea-bed uplift and subsidence. Regarding the amplification coefficient A, it has been found that the faults offshore are the ones that induce initial tsunami waveforms that can be most amplified at the coast.

If the interest is not in tsunami amplification, but in the tsunami inundation potential, then we must discriminate between coastal positive and negative displacements and consider the flooding factors. Permanent subsidence of the shoreline favours inundation which is reflected in flooding factors F_f approaching 1, whereas coastal uplift favours sea retreat and the corresponding drying factors F_d are close to 1.

An extremely relevant result is that none of the quantities we have used to quantify the tsunami effects, namely A, F_f and F_d, depends on the initial tsunami wave height, at least within the range of reasonable heights expected from seismic sources. This property is essential since it enables us to apply the results we obtained for normalized wave profiles to waveforms of arbitrary amplitude.

The effect of the sea-bottom slope on tsunami evolution is a further aspect investigated here, and it is remarkable to have obtained that tsunami amplification is independent of the slope, which instead affects significantly the water speed and the tsunami time scale. Wave periods decrease with the ocean slope, while water velocity increase.

Last, breaking conditions for tsunami waves have been studied through the analysis of the Jacobian of the hodograph transformation. The main results obtained are that tsunamis with initial height less than about 8–9 m do not break, and that tsunamis with a very simple initial profile (that may be attributed to earthquakes with epicentre onshore) do not break even for initial heights as large as 19 m. Such large Earth's surface dislocations cannot be produced by small or medium-size earthquakes. Making recourse to experimental laws giving the co-seismic displacements as a function of the earthquake size, such as the one that was deduced by Wells & Coppersmith (1994), one sees that only very large earthquakes (with moment magnitude $\geqslant 8.5$) can offset the Earth's surface by more than 8 m, and that dislocations exceeding 10–15 m are expected to be generated only by exceptionally large earthquakes (see figure 18). Therefore, we conclude that most tsunamis that are caused by near-shore seismic sources are likely to evolve and attack the coast without breaking.

The research has been funded partly by GNDT-INGV (Gruppo Nazionale Difesa dai Terremoti) and partly by GNV-INGV (Gruppo Nazionale di Vulcanologia) through the Istituto Nazionale di Geofisica e Vulcanologia, Rome, Italy, to study the run-up of tsunamis generated in the near-shore zone.

Appendix A

Displacements and stresses caused by an earthquake in the surrounding medium are difficult to compute, but under the hypothesis that the medium is a perfectly elastic, homogeneous and isotropic half-space, explicit expressions can be provided by dislocation theory both for point sources and for rectangular faults. Full solutions are rather complicated and were published by Okada (1985, 1992) for basic types of source dislocations (strike, dip, tensile and inflation). Here we deduce the expression for the vertical displacement of the Earth's surface for the special case of a dip–slip fault of infinite length. To do so, we start from Okada's solution as is given in table 6 of the 1992 paper, which is valid for a fault of width W and length L. However, with respect to the original paper, we consider here a different orientation of the fault that is aligned with the y^*-axis, and is placed between $-L/2 \leqslant y^* \leqslant L/2$. After some

manipulations, the vertical component of the displacement u_z along the axis x^*, which is taken to be normal to the fault, can be written as

$$u_z(x^*) = \frac{U}{2\pi}[U_S(x^*)\sin\delta + U_C(x^*)\cos\delta]. \tag{A 1}$$

Here U is the slip on the fault and δ the dip angle, that is the angle the fault forms with the horizontal plane, as is usual. The functions $U_S(x^*)$ and $U_C(x^*)$ are given by

$$\left.\begin{aligned} U_S(x^*) = \Bigg\{ &-\frac{\eta q}{R(R+\xi)} - \arctan\left(\frac{\eta\xi}{qR}\right) \\ &+ 2(1-2\nu)\arctan\left(\frac{\eta(X+q\cos\delta)+X(R+X)\sin\delta}{\xi(R+X)\cos\delta}\right)\Bigg\}\Bigg\| \quad \text{if } \delta \neq \tfrac{1}{2}\pi, \\ U_S(x^*) = \Bigg\{ &-\frac{\eta q}{R(R+\xi)} - \arctan\left(\frac{\eta\xi}{qR}\right)\Bigg\}\Bigg\| \qquad \text{if } \delta = \tfrac{1}{2}\pi, \end{aligned}\right\} \tag{A 2}$$

$$U_C(x^*) = \left\{ -\frac{q^2}{R(R+\xi)}\right\}\Bigg\|, \tag{A 3}$$

where the double bar symbol has the following meaning:

$$\{f(\xi,\eta)\}\| = f(L/2, p) - f(L/2, p-W) - f(-L/2, p) + f(-L/2, p-W), \tag{A 4}$$

and X, R, q and p are respectively defined as

$$X^2 = \xi^2 + q^2, \tag{A 5}$$

$$R^2 = \xi^2 + \eta^2 + q^2, \tag{A 6}$$

$$q = x^*\sin\delta - D\cos\delta, \tag{A 7}$$

$$p = x^*\cos\delta + D\sin\delta + W. \tag{A 8}$$

Here D, appearing in the expressions for q and p, is the depth of the upper edge of the fault taken positive downward. Notice that the Poisson coefficient ν is the only elastic parameter influencing the seismic displacement, which indeed is a general property of Okada's solution, but the special case of a vertical fault ($\delta = \pi/2$), $u_z(x^*)$ is found to be independent even of ν. After some algebraic computations, consisting in performing the calculations implied by the double bar symbol and in letting the fault length L go to infinity, the displacement $u_z(x^*)$ can be written simply as

$$u_z(x^*) = \frac{U}{\pi}\left[U_S^\infty(x^*)\sin\delta + U_C^\infty(x^*)\cos\delta\right], \tag{A 9}$$

$$U_S^\infty(x^*) = \frac{pq}{p^2+q^2} - \frac{(p-W)q}{(p-W)^2+q^2} + \arctan\left(\frac{p-W}{q}\right) - \arctan\left(\frac{p}{q}\right), \tag{A 10}$$

$$U_C^\infty(x^*) = -\frac{q^2}{p^2+q^2} + \frac{q^2}{(p-W)^2+q^2}, \tag{A 11}$$

where the dependence on x^* is implicit in the functions q and p in expressions (A 7) and (A 8). Notably, the above formula reveals that the vertical displacements are, surprisingly, independent of the elastic parameters of the medium for a fault that is infinitely long. Notice further that here the origin of the horizontal axis is taken to coincide with the position of the projection of the upper edge of the fault. For a vertical fault ($\delta = \pi/2$), the expression simplifies further, becoming

$$u_z(x^*) = \frac{U}{\pi}\left[\frac{x^*(D+W)}{x^{*2}+(D+W)^2} - \frac{x^*D}{x^{*2}+D^2} + \arctan\left(\frac{D}{x^*}\right) - \arctan\left(\frac{D+W}{x^*}\right)\right], \tag{A 12}$$

$$u_z(0) = 0.$$

When the slip U is positive, the block on the right-hand side of the fault, i.e. on the side of increasing $x*$, moves downward, causing subsidence, while the block on the opposite side of the fault goes upward. In this paper, the initial sea level elevation for the tsunami has been assumed to be equal to the sea-bottom vertical displacement, which implies that

$$\eta^*(x^*, t^* = 0) = u_z(x^*). \tag{A 13}$$

Appendix B

The inner integral of equations (3.17) and (3.18) is

$$\int_0^\infty \sigma_0^2 J_1(\tau\sigma_0) f(\sigma_0)\,\mathrm{d}\sigma_0.$$

If use is made of the expression (3.21) for $f(\sigma_0)$, the above integral can be calculated easily:

$$\begin{aligned}\int_0^\infty \sigma_0^2 J_1(\tau\sigma_0) f(\sigma_0)\,\mathrm{d}\sigma_0 &= -8\int_0^\infty \frac{\sigma_0^2 J_1(\tau\sigma_0)}{\left(1+\sigma_0^2\right)^{5/2}}\left[\sum_{k=0}^{3} c_k \frac{(k+3/2)}{\left(1+\sigma_0^2\right)^k}\right]\mathrm{d}\sigma_0 \\ &= -8\sum_{k=0}^{3} c_k (k+3/2)\int_0^\infty \frac{\sigma_0^2 J_1(\tau\sigma_0)}{\left(1+\sigma_0^2\right)^{k+5/2}}\,\mathrm{d}\sigma_0 \\ &= -8\sum_{k=0}^{3} c_k (k+3/2)\frac{\tau^{k+3/2}}{2^{k+3/2}\Gamma(k+5/2)} K_{k+1/2}(\tau)\end{aligned} \tag{B 1}$$

where $K_\nu(\tau)$ is the Bessel function of imaginary argument that is related to Hankel's function as follows (Gradshteyn & Ryzhik 1965):

$$K_\nu(\tau) = \frac{\pi \mathrm{i}}{2}\,\mathrm{e}^{\pi\nu\mathrm{i}/2} H_\nu^{(1)}(\mathrm{i}\tau).$$

Since $K_\nu(\tau)$, when the order is equal to an integer plus one-half, can be given the form

$$K_{k+1/2}(\tau) = \sqrt{\frac{\pi}{2\tau}}\,\mathrm{e}^{-\tau}\sum_{j=0}^{k}\frac{(k+j)!}{j!(k-j)!(2\tau)^j} \tag{B 2}$$

expressions (3.17) and (3.18) can be rewritten in the following way:

$$\begin{aligned}v(\sigma,\lambda) = &-\frac{8}{\sigma}\sqrt{\frac{\pi}{2}}\sum_{k=0}^{3}\frac{c_k(k+3/2)}{2^{k+3/2}\Gamma(k+5/2)} \\ &\times\sum_{j=0}^{k}\frac{(k+j)!}{j!(k-j)!2^j}\int_0^\infty J_1(\tau\sigma)\sin(\tau\lambda)\,\tau^{k-j+1}\mathrm{e}^{-\tau}\,\mathrm{d}\tau,\end{aligned} \tag{B 3}$$

$$\begin{aligned}\phi(\sigma,\lambda) = &\;8\sqrt{\frac{\pi}{2}}\sum_{k=0}^{3}\frac{c_k(k+3/2)}{2^{k+3/2}\Gamma(k+5/2)} \\ &\times\sum_{j=0}^{k}\frac{(k+j)!}{j!(k-j)!2^j}\int_0^\infty J_0(\tau\sigma)\sin(\tau\lambda)\,\tau^{k-j}\mathrm{e}^{-\tau}\,\mathrm{d}\tau.\end{aligned} \tag{B 4}$$

Correspondingly, the derivative $\phi_\lambda(\sigma, \lambda)$ that is needed to compute the water elevation η, can be put in the form

$$\phi_\lambda(\sigma,\lambda) = 8\sqrt{\frac{\pi}{2}}\sum_{k=0}^{3}\frac{c_k(k+3/2)}{2^{k+3/2}\Gamma(k+5/2)} \times \sum_{j=0}^{k}\frac{(k+j)!}{j!(k-j)!2^j}\int_0^\infty J_0(\tau\sigma)\cos(\tau\lambda)\,\tau^{k-j+1}\mathrm{e}^{-\tau}\,\mathrm{d}\tau. \tag{B 5}$$

The derivatives of the velocity $v(\sigma, \lambda)$ enter the formula of the Jacobian of the hodograph transformation and the analysis of wave breaking. Here only the expression for $v_\lambda(\sigma, \lambda)$ is given, which can be used to calculate the breaking factor K_b^* and which can be easily derived from (B 3):

$$v_\lambda(\sigma,\lambda) = -\frac{8}{\sigma}\sqrt{\frac{\pi}{2}}\sum_{k=0}^{3}\frac{c_k(k+3/2)}{2^{k+3/2}\Gamma(k+5/2)} \times \sum_{j=0}^{k}\frac{(k+j)!}{j!(k-j)!2^j}\int_0^\infty J_1(\tau\sigma)\cos(\tau\lambda)\,\tau^{k-j+2}\mathrm{e}^{-\tau}\,\mathrm{d}\tau. \tag{B 6}$$

If we consider the identities

$$\sin(\tau\lambda)\,\mathrm{e}^{-\tau} = \mathrm{Im}\{\mathrm{e}^{-p\tau}\},$$
$$\cos(\tau\lambda)\,\mathrm{e}^{-\tau} = \mathrm{Re}\{\mathrm{e}^{-p\tau}\},$$

where $p = 1 - \mathrm{i}\lambda$, the integrals contained in formulas (B 3)–(B 6) can be transformed to

$$\int_0^\infty J_1(\tau\sigma)\sin(\tau\lambda)\,\tau^{k-j+1}\mathrm{e}^{-\tau}\,\mathrm{d}\tau = \mathrm{Im}\left\{\int_0^\infty J_1(\tau\sigma)\,\tau^{k-j+1}\mathrm{e}^{-p\tau}\,\mathrm{d}\tau\right\},$$
$$\int_0^\infty J_1(\tau\sigma)\cos(\tau\lambda)\,\tau^{k-j+2}\mathrm{e}^{-\tau}\,\mathrm{d}\tau = \mathrm{Re}\left\{\int_0^\infty J_1(\tau\sigma)\,\tau^{k-j+2}\mathrm{e}^{-p\tau}\,\mathrm{d}\tau\right\},$$
$$\int_0^\infty J_0(\tau\sigma)\sin(\tau\lambda)\,\tau^{k-j}\mathrm{e}^{-\tau}\,\mathrm{d}\tau = \mathrm{Im}\left\{\int_0^\infty J_0(\tau\sigma)\,\tau^{k-j}\mathrm{e}^{-p\tau}\,\mathrm{d}\tau\right\},$$
$$\int_0^\infty J_0(\tau\sigma)\cos(\tau\lambda)\,\tau^{k-j+1}\mathrm{e}^{-\tau}\,\mathrm{d}\tau = \mathrm{Re}\left\{\int_0^\infty J_0(\tau\sigma)\,\tau^{k-j+1}\mathrm{e}^{-p\tau}\,\mathrm{d}\tau\right\}.$$

All these integrals are of the same type and can be computed by means of the general formula

$$\int_0^\infty x^{m+1}\mathrm{e}^{-\alpha x}J_\nu(\beta x)\,\mathrm{d}x = (-1)^{m+1}\beta^{-\nu}\frac{\mathrm{d}^{m+1}}{\mathrm{d}\alpha^{m+1}}\left[\frac{(\sqrt{\alpha^2+\beta^2}-\alpha)^\nu}{\sqrt{\alpha^2+\beta^2}}\right]$$

holding when the following inequalities are fulfilled: $\beta > 0$, $\mathrm{Re}\{\nu\} > -m-2$ (Gradshteyn & Ryzhik 1965), which is true in the present case.

REFERENCES

Altinok, Y., Tinti, S., Alpar, B., Ersoy, S., Yalçiner, A. C., Bortolucci, E. & Armigliato, A. 2001 The tsunami of August 17, 1999 in the Izmit Bay; Turkey. *Natural Hazards* **24**, 133–146.

Carrier, G. F. & Greenspan, H. P. 1958 Water waves of finite amplitude on a sloping beach. *J. Fluid Mech.* **4**, 97–110.

Carrier, G. F. 1971 The dynamics of tsunamis. In *Mathematical Problems in Geophysical Sciences: 1. Geophysical Fluid Dynamics* (ed. W. H. Reid), pp. 157–187. American Mathematical Society.

Carrier, G. F., Wu, T. T. & Yeh, H. 2003 Tsunami run-up and draw-down on a plane beach. *J. Fluid Mech.* **475**, 79–99.

Geist, E. L., Kikuchi, M., Hirata, K., Yoshioka, S. & Bilek, S. 2001 Modeling the 23 June 2001 Peru local tsunami using results from a quick seismic inversion of the earthquakes. *Proc. Intl Tsunami Symposium, Seattle, Washington.* 411–412.

Gradshteyn, I. S. & Ryzhik, I. M. 1965 *Table of Integrals, Series, and Products.* Academic Press.

Hanks, T. C. & Kanamori, H. 1979 A moment-magnitude scale. *J. Geophys. Res.* **84**, 2348–2350.

Hokkaido Tsunami Survey Group 1993 Tsunami devastates Japanese coastal Regions. *EOS, Trans. AGU* **74**, 417–432.

International Survey Team 2001 Impacts of the 2001 Peru tsunami in Camana. *Proc. Intl Tsunami Symposium, Seattle, Washington.* 409.

Kânoğlu, U. 2004 Nonlinear evolution and runup-rundown of long waves over a sloping beach. *J. Fluid Mech.* **513**, 363–372.

Liu, P. L.-F., Lynett, P. & Synolakis, C. E. 2003 Analytical solutions for forced long waves on a sloping beach. *J. Fluid Mech.* **478**, 101–109.

Maramai, A., Graziani, L. & Tinti, S. 2003 Updating and revision of the European tsunami catalogue. In *Submarine Landslides and Tsunamis* (ed. A. C. Yalçiner, E. N. Pelinovsky, E. Okal & C. E. Synolakis), pp. 25–32. Kluwer.

Okada, Y. 1985 Surface deformation due to shear and tensile faults in a half-space. *Bull. Seismol. Soc. Am.* **75**, 1135–1154.

Okada, Y. 1992 Internal deformation due to shear and tensile faults in a half-space. *Bull. Seismol. Soc. Am.* **82**, 1018–1040.

Pelinovsky, E. N. & Mazova, K. H. 1992 Exact solutions of nonlinear problems of tsunami wave run-up on slopes with different profiles. *Natural Hazards* **6**, 227–249.

Preuss, J., Raad, P. & Bidoae, R. 2001 Mitigation strategies based on local tsunami effects. In *Tsunami Research at the End of a Critical Decade* (ed. G. T. Hebenstreit). *Advances in Natural and Technological Hazards Research.* Kluwer.

Shuto, N. & Matsutomi, H. 1995 Field survey of the 1993 Hokkaido Nansei-Oki tsunami. *Pure Appl. Geophys.* **144** (3/4), 649–664.

Soloviev, S. L., Go, Ch. N., Kim, Kh. S., Solovieva, O. N. & ShChetnikov, N. A. 2000 *Tsunamis in the Mediterranean Sea, 2000 B.C.-2000 A.D.*, p. 236. Kluwer.

Spielvogel, L. Q. 1975 Single-wave run-up on sloping beaches. *J. Fluid Mech.* **74**, 685–694.

Synolakis, C. E. 1987 The run-up of solitary waves. *J. Fluid Mech.* **185**, 523–545.

Synolakis, C. E. 1991 Tsunami run-up on steep slopes: how good linear theory really is. *Natural Hazards* **4**, 221–234.

Tadepalli, S. & Synolakis, C. E. 1994 The run-up of N-waves on sloping beaches. *Proc. R. Soc. Lond.* A **445**, 99–112.

Tinti, S. & Maramai, A. 1996 Catalogue of tsunamis generated in Italy and in Côte d'Azur, France: a step towards a unified catalogue of tsunamis in Europe. *Annali di Geofisica* **39**, 1253–1299.

Tinti, S., Maramai, A. & Graziani, L. 2004 The new catalogue of the Italian tsunamis. *Natural Hazards* **33**, 439–465.

Trifunac, M. D. & Todorovska, M. I. 2003 Tsunami source parameters of submarine earthquakes and slides. In *Submarine Mass Movements and Their Consequences* (ed. J. Locat & J. Mienert), *Advances in Natural and Technological Hazards Research.* vol. 19, pp. 121–128. Kluwer.

Wells, D. L. & Coppersmith, K. J. 1994 New empirical relationships among magnitude, rupture length, rupture width, rupture area, and surface displacement. *Bull. Seismol. Soc. Am.* **84**(4), 974–1002.

Yalçiner, A. C., Synolakis, C. E., Alpar, B., Borrero, J. C., Altinok, Y., Imamura, F., Tinti, S., Ersoy, S., Kuran, U., Pamukcu, S. & Kanoglu, U. 2001 Field surveys and modeling of the 1999 Izmit tsunami. *International Tsunami Symposium Proc., Seattle, August 7-10 2001.* 557–563.

Yeh, H. H., Imamura, F., Synolakis, C. E., Tsuji, Y., Liu, P. & Shi, S. 1993 The Flores Island Tsunami. *EOS, Trans. AGU* **74**, 369, 371–373.